МІНІСТЕРСТВО ОСВІТИ І НАУКИ УКРАЇНИ
ХАРКІВСЬКИЙ НАЦІОНАЛЬНИЙ УНІВЕРСИТЕТ
імені В. Н. Каразіна
Кафедра неорганічної хімії
РУРСЬКИЙ УНІВЕРСИТЕТ
Кафедра теоретичної хімії II

УДК 544.225

До захисту допускаю
_____ Завідувач кафедри
к.х.н., доц. М. М. Волобуєв
«16» травня 2025 р.

ДОСЛІДЖЕННЯ ОКСИДУ ЦИНКУ, ЛЕГОВАНОГО МАРГАНЦЕМ, МЕТОДОМ ТЕОРІЇ ФУНКЦІОНАЛУ ГУСТИНИ

Кваліфікаційна робота магістра
II курсу хімічного факультету
ГРИЦЕНКА БОГДАНА ЮРІЙОВИЧА

Науковий керівник
к.х.н., професор Олег КАЛУГІН
доктор, професор Йорг БЕЛЕР

ХАРКІВ/БОХУМ 2025

MINISTRY OF EDUCATION AND SCIENCE OF UKRAINE
V. N. KARAZIN KHARKIV NATIONAL UNIVERSITY
Department of Inorganic Chemistry
RUHR-UNIVERSITÄT BOCHUM
Theoretical Chemistry II Department

UDC 544.225

Admitted to the defense
_ _____ Head of the Department,
PhD in Chemistry, Associate Professor M. M. Volobuev
«16» 05 2025

DENSITY FUNCTIONAL THEORY INVESTIGATION OF MN-DOPED ZINC OXIDE

Master's Qualification Thesis
2nd-year student of the Faculty of Chemistry
BOHDAN Y. HRYTSENKO

Supervisor
PhD, Professor — Oleg KALUGIN
Doctor, Professor — Jörg BEHLER

KHARKIV/BOCHUM 2025

РЕФЕРАТ

Дана магістерська кваліфікаційна робота обсягом 47 сторінок включає в себе теоретичний огляд, розділ методології та аналіз результатів. Робота містить 22 рисунка, 3 таблиці, 1 додаток та 50 літературне джерело.

Робота присвячена теоретичному дослідженню оксиду цинку (ZnO), легованого марганцем (Mn), із застосуванням методів теорії функціоналу густини (DFT). Об'єктом дослідження виступають об’ємні та поверхневі (slab) моделі ZnO, в яких розглядалася поведінка Mn-допанту в різних кристалографічних положеннях. Основну увагу приділено порівнянню функціоналів GGA (optPBE), DFT+U (optPBE+U) та гібридного PBE0 щодо опису електронної структури, густини станів і магнітних властивостей системи.

Метою є аналіз залежних від положення ефектів легування ZnO манганом на його структурні та електронні властивості у поєднанні з оцінкою методу DFT+U у порівнянні з гібридними функціоналами, закладаючи основу для розробки потенціалів машинного навчання для великомасштабного моделювання інтерфейсів Mn/ZnO, зокрема у системах ZnO–вода.

У роботі проведено геометричну оптимізацію, розрахунки енергетики, електронної густини станів (DOS/PDOS) та аналіз впливу параметрів Хаббарда (U) на електронну структуру легованого ZnO. Показано, що метод DFT+U (U(Zn)=4 eB, U(Mn)=2 eB) забезпечує близькі до гібридного функціоналу результати при значно нижчих обчислювальних витратах. Проведено аналіз впливу ініціалізації магнітного моменту (MAGMOM) на точність моделювання спінових станів Mn. У slab-моделях встановлено термодинамічну перевагу поверхневого розміщення атома Mn, що має важливе значення для каталітичних застосувань. Результати роботи є цінною основою для подальшого моделювання взаємодії ZnO з водою з використанням методів машинного навчання та розробки функціональних матеріалів нового покоління.

Ключові слова: МАРГАНЕЦЬ, ОКСИД ЦИНКУ, ЛЕГУВАННЯ, DFT+U, PBE0, ТЕОРІЯ ФУНКЦІОНАЛУ ГУСТИНИ, МАГНІТНІ ВЛАСТИВОСТІ, ГУСТИНА СТАНІВ, SLAB-МОДЕЛІ, ПОВЕРХНЕВА ЕНЕРГЕТИКА.

ABSTRACT

This master's thesis consists of 47 pages and includes a theoretical overview, a methodology section, and an analysis of results. The work contains 22 figures, 3 tables, 1 appendix, and 50 references.

The study is devoted to the theoretical investigation of zinc oxide (ZnO) doped with manganese (Mn) employing density functional theory (DFT) methodologies. The research focuses on both bulk and surface (slab) models of ZnO, examining the behavior of Mn dopants at various crystallographic positions. Comparisons are made between the performance within the GGA (optPBE), DFT+U (optPBE+U), and hybrid (PBE0) functionals in terms of defining the electronic structure by means of density of states, and magnetic characteristics.

The aim is the analysis the site-dependent effects of Mn doping on the structural and electronic properties of zinc oxide ZnO is combined with an evaluation of the DFT+U method versus hybrid functionals, providing a foundation for the development of machine learning potentials for large-scale simulations of Mn/ZnO interfaces, particularly ZnO–water systems.

The work includes geometry optimization, total energy calculations, electronic density of states (DOS/PDOS) analysis, and an evaluation of the effect of Hubbard U parameters on the electronic structure of Mn-doped ZnO. It is shown that the DFT+U method (with U(Zn) = 4 eV and U(Mn) = 2 eV) yields results comparable to hybrid functionals while significantly reducing computational costs. The influence of initial magnetic moment (MAGMOM) initialization on the accurate modeling of Mn spin states is also analyzed. In the slab models, a thermodynamic preference for surface substitution of Mn atoms was established, which is particularly important for catalytic applications. The findings of this work provide a valuable foundation for further modeling of ZnO–water interactions using machine learning methods and for the design of next-generation functional materials.

Keywords: MANGANESE, ZINC OXIDE, DOPING, DFT+U, PBE0, DENSITY FUNCTIONAL THEORY, MAGNETIC PROPERTIES, DENSITY OF STATES, SLAB MODELS, SURFACE ENERGETICS.

TABLE OF CONTENTS

INTRODUCTION

Zinc oxide (ZnO) is a type of material of significant scientific interest due to its wide band gap of approximately 3.37 eV and an immense excitation binding energy of about 60 meV, combined with outstanding thermal and chemical stability[1-3]. The subsequent argumentation will look at the strategies by which ZnO is indispensable for applications in optoelectronics, photocatalysis and transparent conducting oxides[4-5]. The development of modern technologies relies on these three areas, and thus ZnO is an essential component in this field.

ZnO can be synthesised in various forms, including nanoparticles, nanorods, nanowires, nanoflowers, and 2D nanosheets[6-7]. It has been demonstrated that the synthesis method and specific conditions – such as pH, temperature, and capping agents, significantly affect the morphology and properties of the resulting material[8-9]. ZnO can be produced through a diversity of procedures, including sol-gel, hydrothermal, solvothermal, and mechanochemical processes[10]. The selection of methodology exerts a considerable influence on the characteristics of the resulting particles, including their size, shape, and functional behaviour, such as photocatalytic efficiency and surface activity.

Furthermore, the doping of ZnO with different elements – or even the co-doping of multiple dopants – enables precise calibration of its optical, electrical, magnetic, and photocatalytic properties[11-13]. For instance, the addition of transition metals such as manganese, cobalt, or nickel can result in the manifestation of magnetic behaviour, while rare-earth metals have been found to stimulate their ability to function as luminescent [14-15]. This renders ZnO a flexible and multifunctional material suitable for next-generation applications in fields ranging from photovoltaics and gas sensing to antimicrobial coatings and biomedical imaging[16]. ZnO has been revealed to exhibit piezoelectric and pyroelectric properties, which enable the generation of electric charges in response to mechanical stress or temperature changes. This renders it a valuable material for applications such as energy harvesting devices and smart sensors[17-18].

Mn-doped ZnO materials have attracted significant research interest due to their modified structural, optical, electrical, magnetic, and photocatalytic properties[19-20]. Doping ZnO with manganese alters its characteristics, making it suitable for multiple

uses, notably photocatalysis, optoelectronics, spintronics, and energy storage[21]. Manganese doping has been depicted to markedly boost the reactive capacity of zinc oxide and encourage the oxygen evolution process[22]. It was properly highlighted that, under typical circumstances, Mn-doped ZnO exhibits a hexagonal wurtzite structure, with Mn ions substituting Zn in the lattice without forming secondary impurity phases at moderate doping levels[23]. The significance of supplementing grain growth is well documented, with the process of increasing grain size and promoting grain boundary diffusion being especially pronounced at higher Mn concentrations. Morphological changes have been observed, including transformation from nanosheets to nanorods and nanoparticles as the Mn content increases[19, 24]. The following discussion will address defects and strain. The integration of manganese into the ZnO lattice has been shown to increase defect sites, dislocation density, and microstrain. These changes have the potential to affect the material's physical and functional qualities. At low concentrations, the material exhibits a tendency to reduce the band gap, therefore increasing its ability to absorb visible light. Nonetheless, it has been demonstrated that, under conditions of elevated Mn concentration, there may be an augmentation of the width of band gap[20, 25-26]. From an electrical standpoint, the addition of manganese (Mn) to a substance typically results in an enhancement of resistivity and a reduction in charge carrier mobility, particularly as the quantity of Mn increases.

The ZnO-water interface plays a crucial role in various advanced applications due to its unique surface chemistry, which allows for both molecular and dissociative adsorption of water. This mixed adsorption behavior is central to ZnO’s effectiveness in fields such as medicinal chemistry, biosensors, pH sensors, and catalysis. The interface between ZnO and water is critical for photocatalytic degradation of pollutants. Modifications such as forming heterojunctions with other materials or doping with metals enhance charge separation and interfacial reactions, leading to higher efficiency in water splitting[27-28].

Standard generalized gradient approximation (GGA) functionals in density functional theory (DFT) often struggle to accurately describe the electronic structure of ZnO, primarily due to the presence of localized Zn 3d orbitals. This leads to significant underestimation of the band gap and incorrect positioning of d-states in ZnO[29-31].

The DFT+U method is an extension of standard density functional theory (DFT) that sets up a Hubbard correction (the parameter U) to better account for strong electron-electron interactions, especially in systems with localized electrons such as transition metal oxides[32]. This correction helps overcome DFT's limitations in describing correlated materials, leading to more accurate predictions of electronic, structural, and spectroscopic properties. It is particularly effective for systems with d- or f-electrons, such as transition metal oxides and rare-earth compounds[30-31]. DFT+U modifies the energy functional by penalizing fractional occupancies in localized orbitals, thereby better capturing strong correlation effects. The preciseness of DFT+U strongly depends on the value of the Hubbard U parameter. Methods to determine U include linear response calculations and machine learning approaches, such as Bayesian optimization, which can yield U values that closely reproduce results from more accurate but computationally expensive methods. The choice of local orbitals (the subspace where U is applied) significantly affects the results, especially in systems with strong covalent bonding[33].

Object: The object of this research is manganese-doped zinc oxide in both bulk and slab (surface) geometries. The study focuses on understanding how Mn substitution affects the structural, electronic, magnetic, and surface properties of ZnO using state-of-the-art quantum mechanical simulations. Particular emphasis is placed on the influence of Mn dopants under different concentrations and crystallographic positions.

Method: The study employs density functional theory (DFT) calculations effectuated with the Vienna *Ab initio* Simulation Package (VASP), using both GGA-based functionals (optPBE) and Hubbard U-corrected approaches (DFT+U), in spite of hybrid functionals (PBE0, HSE06). A key methodological aspect is the application and tuning of U parameters and the proper initialization of magnetic moments via the MAGMOM tag to describe the high-spin d^5 configuration of Mn. Surface slab models of the ZnO plane were constructed and analyzed with Mn dopants placed in six distinct substitutional positions.

Aim: Analysis of the site-dependent effects of Mn doping on the structural and electronic properties of ZnO is combined with an evaluation of the DFT+U method versus hybrid functionals, providing a foundation for the development of machine

learning potentials for extensive simulations of Mn/ZnO interfaces, particularly ZnO–water systems.

Tasks:

1) To optimize computational parameters (ENCUT, k-point mesh, spin initialization) for both pure and Mn-doped ZnO systems.
2) To determine the optimal value of the Hubbard + U parameter by analyzing 16 different DFT+U configurations and visually comparing the resulting density of states (DOS) with those obtained using hybrid functionals.
3) To perform DFT+U calculations for bulk ZnO using supercells of various sizes (2×2×2, 3×3×1, 4×2×1) with single Mn dopants, simulating different concentrations.
4) To analyze the total and projected density of states (DOS/PDOS) for both non-magnetic and spin-polarized configurations and assess the role of MAGMOM initialization.
5) To compare DFT+U results with hybrid functional results (PBE0, HSE06) concerning correctness and computational cost.
6) To construct and relax slab models of the ZnO surface and calculate relative replacement energies of Mn at six distinct Zn locations.
7) To detect through thermodynamics favoured dopant spot.

CHAPTER 1. THEORY REVIEW

1.1 First-Principles Methods

First-principles methods are grounded in quantum mechanics, offering a rigorous description of the interactions between electrons and atomic nuclei within various systems. The cornerstone of these methods is the Schrödinger equation, which determines the quantum state of a system:

$$\hat{H}\Psi = E\Psi, \tag{1.1}$$

where $\hat{H}$ represents the Hamiltonian operator, Ψ is the wavefunction, E denotes the total energy of the system[34]. The Hamiltonian operator spans both the kinetic and potential energy contributions arising from Coulombic interactions among electrons and nuclei. Its explicit form is:

$$\hat{H} = \sum_I \frac{\widehat{P_I^2}}{2M_I} + \sum_i \frac{\widehat{p_i^2}}{2m_i} + \sum_{I<J} \frac{Z_I Z_J e^2}{|R_I - R_J|} + \sum_{i<j} \frac{e^2}{|r_i - r_j|} - \sum_{I,i} \frac{Z_I e^2}{|R_I - r_i|}, \tag{1.2}$$

where P_I and p_i are the momentum operators for nuclei and electrons, correspondingly, while R_I and r_i indicate their spatial coordinates. Z_I is the nuclear charge, e is the elementary charge, and M_I , m_i denote the masses of nuclei and electrons[35].

The direct solution of the Schrödinger equation for systems with multiple interacting electrons is computationally infeasible due to the many-body nature of the problem and the exponential scaling of complexity with system size. Practical applications in computational and theoretical chemistry, therefore, rely on methods that are computationally efficient and scalable, as will be elaborated in the following discussion.

1.2 Density Functional Theory

Density Functional Theory (DFT), based on the pioneering contributions of Hohenberg and Kohn in 1964, transformed the understanding of many-electron systems by introducing a framework predicated on the electron density, ρ(r). The principles of

DFT were established by the groundbreaking work of Hohenberg and Kohn(1964), encapsulated in two key theorems:

1. The ground-state properties of a many-electron system is uniquely defined by its electron density ρ(r). This indicates that all information on the system, including its energy and wavefunction, may be articulated as functionals of ρ(r).
2. The ground-state electron density ρ(r) reduces the energy functional E[ρ], guaranteeing that actual ground-state energy aligns with the lowest value of E[ρ].

The electron density is formally defined as:

$$\rho(r) = N \int \Psi^*(r_1, r_2, \dots, r_N)\Psi(r_1, r_2, \dots, r_N)\ dr_2\ \dots\ dr_N, \tag{1.3}$$

where Ψ is the many-body wavefunction, N is the total number of electrons, and r_i represents the spatial coordinates of the i-th electron. The total energy of the system is expressed as a functional of the electron density:

$$E[\rho] = T[\rho] + V_{Ne}[\rho] + V_{ee}[\rho], \tag{1.4}$$

where $T[\rho]$ denotes the kinetic energy of the electrons, $V_{Ne}[\rho]$ is the electron-nuclear attraction energy, and $V_{ee}[\rho]$ accounts for the electron-electron repulsion[36].

Building upon this foundation, Kohn and Sham(1965) introduced a method to simplify the treatment of many-body systems by proposing a fictitious system of non-interacting electrons reproducing the same ground-state density as the interacting system. Under the Kohn–Sham formalism, the total energy can be stated as:

$$E[\rho] = T_s[\rho] + \int v_{ext}(r)\rho(r)\ dr + E_{XC}[\rho], \tag{1.5}$$

where $T_s[\rho]$ denotes the kinetic energy of the non-interacting reference system, $v_{ext}(r)$ is the external potential due to the nuclei, and $E_{XC}[\rho]$ represents the exchange-correlation energy, which encapsulates the effects of electron exchange and correlation. The exact form of the exchange-correlation functional $E_{XC}[\rho]$ is unknown, and practical applications of DFT rely on approximations[37]. Commonly employed approaches include the Local Density Approximation (LDA) and the Generalized Gradient Approximation (GGA), which offer varying degrees of accuracy depending on the system under study. Despite its approximations, DFT has become a cornerstone of

modern quantum chemistry and materials science, providing a balance between computational efficiency and accuracy[38].

1.3 Exchange–Correlation Functional in DFT

The exchange–correlation functional, $E_{XC}[\rho]$, is a fundamental component of DFT, evaluating the many-body effects of electron migration and correlation effects. Since the exact form of $E_{XC}[\rho]$ remains unknown, practical applications rely on approximations. Two of the most frequently applied approximations are the Local Density Approximation (LDA) and the Generalised Gradient Approximation (GGA), both of which offer a balance between computational efficiency and accuracy. The Local Density Approximation posits that the exchange–correlation energy relies only on the local electron density ρ(r), as if the system were a homogeneous electron gas[38]. The exchange–correlation energy functional in LDA is defined as:

$$\mathrm{E}_{\mathrm{XC}}^{\mathrm{LDA}}[\rho] = \int \epsilon_{\mathrm{XC}}^{\mathrm{hom}}[\rho(\mathrm{r})]\rho(\mathrm{r})\ \mathrm{dr}, \tag{1.6}$$

where $\epsilon_{\mathrm{XC}}^{\mathrm{hom}}[\rho(\mathrm{r})]$ is the exchange–correlation energy density of a uniform electron gas at the local density ρ(r). The LDA is particularly effective for materials with nearly uniform or slowly varying electron densities, such as simple metals and some semiconductors. However, its inherent limitations become apparent in systems with strongly localized electrons or significant electron density variations. For example, LDA often struggles to accurately describe systems with strongly correlated electrons, such as transition metal oxides, leading to significant deviations from experimental results. Similarly, the GGA, which improves upon LDA by incorporating density gradients, also fails to fully capture the complex interactions in these materials. Both LDA and GGA are insufficient for describing the strongly localized d-electrons in transition metal oxides like ZnO, necessitating the use of more advanced approaches, such as the DFT+U method[30]. The Generalized Gradient Approximation extends the LDA by incorporating the gradient of the electron density, ∇ρ(r), to account for inhomogeneities in the system. The GGA functional is expressed as:

$$E_{XC}^{GGA}[\rho] = \int f[\rho(r), \nabla\rho(r)]\, dr, \quad (1.7)$$

where $f[\rho(r), \nabla\rho(r)]$ is a functional that includes both the local density and its gradient. The inclusion of the gradient term enables GGA to provide a more accurate description of systems with varying electron densities, such as molecular systems, surfaces, and semiconductors. Notable examples of GGA functionals include the Perdew–Burke–Ernzerhof (PBE)[39] functional and its solid-state variant, PBE_{sol} [40]. GGA is widely applied in computational studies of ZnO and similar materials, where electron density variations play a critical role in determining electronic and structural properties. Despite their widespread use, both approximations have limitations, particularly for strongly correlated materials or systems requiring precise treatment of exchange and correlation effects. This has motivated the development of more advanced methods, such as meta-GGA and hybrid functionals, which incorporate higher-order corrections and exact exchange terms. These methods, though computationally more demanding, provide enhanced accuracy for challenging systems. Hybrid functionals, in particular, provide a thorough classification of transition-metals compounds, due to their ability to account for localized d-orbitals. However, this comes at a significant increase in computational expense, and many problems require computationally cheaper methods.

1.4 Hubbard-U Scheme

For systems exhibiting strongly localized electrons, such as ZnO, the conventional LDA and GGA often underestimate the bandgap and fail to accurately describe electronic properties. To address these limitations without resorting to very expensive hybrid functionals, the Hubbard-U correction was introduced, incorporating an on-site Coulomb interaction term, U, into the exchange–correlation functional. The Hubbard-U corrected functional is expressed as:

$$E_{XC}^{LDA+U} = E_{XC}^{LDA} + E_U - E_{dc}, \quad (1.8)$$

where E_U is the additional energy contribution accounting for the on-site Coulomb repulsion of localized electrons, and E_{dc} is a double-counting correction that removes

redundant interactions already included in the LDA functional[41]. In the approach introduced by Dudarev et al.[30], the energy functional is given by:

$$E_{\mathrm{DFT+U}} = E_{\mathrm{LDA}} + \frac{U-J}{2}\sum_{\sigma}\left[\sum_{m_1} n^{\sigma}_{m_1,m_1} - \sum_{m_1,m_2} n^{\sigma}_{m_1,m_2} n^{\sigma}_{m_2,m_1}\right], \quad (1.9)$$

where U and J are the on-site Coulomb and exchange interaction parameters, respectively, and $n^{\sigma}_{m_1,m_1}$ is the occupation matrix for electrons in orbital m with spin σ. This method may be thought of as the introduction of a penalty functional that enforces idempotency of the on-site occupancy matrix :

$$\widehat{n^{\sigma}} = \widehat{n^{\sigma}}\widehat{n^{\sigma}}, \quad (1.10)$$

ensuring that the eigenvalues of the occupancy matrix correspond to fully occupied or fully unoccupied states. The Hubbard-U correction is widely implemented in computational packages such as VASP, offering a practical and computationally efficient efficient strategy to better the electronic structure of compounds with strongly correlated electrons. For ZnO, this correction effectively adjusts the position of the d-states, leading to an improved description of the bandgap and other electronic properties that are not well captured by LDA or GGA alone. Despite its advantages, the Hubbard-U approach requires careful parameterization, which can introduce ambiguity and system dependency.

1.5 The Projector-Augmented Wave (PAW) method

The Projector-Augmented Wave (PAW) The technique, executed inside the Vienna Ab-initio Simulation Package (VASP), is a computational methodology that integrates aspects of ultrasoft pseudopotentials and the linearized augmented-plane-wave (LAPW) method. Initially introduced by Blöchl in 1994[42] and refined by Kresse and Joubert in 1999[43], it has grown into a conventional approach for first-principles computations in density functional theory (DFT). The PAW method reconstructs computationally efficient pseudo-wavefunctions into accurate all-electron wavefunctions ψ through the linear relationship:

$$|\psi_{n\mathbf{k}}\rangle = |\widetilde{\psi}_{n\mathbf{k}}\rangle + \sum_i \left(|\phi_i\rangle - |\widetilde{\phi}_i\rangle\right)\langle \tilde{p}_i|\widetilde{\psi}_{n\mathbf{k}}\rangle \quad (1.11)$$

where $|\phi_i\rangle$ are the all-electron partial waves, $|\widetilde{\phi_i}\rangle$ are the pseudo partial waves, and $\langle\widetilde{p_i}|$ are the projector functions. This formulation enables accurate reconstruction of wavefunctions while maintaining computational efficiency. The total electron density n(r) in the PAW method is expressed as:

$$n(r) = \tilde{n}(r) - \widetilde{n_1}(r) + n_1(r), \tag{1.12}$$

where $\tilde{n}(r)$ indicates the uniform pseudo charge density, $\widetilde{n_1}(r)$ the one-center pseudo charge density, and $n_1(r)$ the one-center all-electron charge density. This partitioning facilitates efficient treatment of core and valence electron densities. The pseudo wavefunctions are expanded in reciprocal arrangement as:

$$\langle r|\widetilde{\psi_{nk}}\rangle = \frac{1}{\sqrt{\Omega}}\sum_G C_{nkG} e^{i(G+k)\cdot r}, \tag{1.13}$$

where G are the reciprocal lattice vectors, k the k-point index, and C_{nkG} the expansion coefficients. In VASP, the frozen-core approximation is employed, where core electron configurations remain fixed, greatly lowering computational expenses while maintaining elevated accuracy. The PAW method is highly accurate, reproducing results close to all-electron calculations while reducing computational cost via pseudo wavefunctions and the frozen-core approximation. It is a versatile method applicable to various systems, including metals, semiconductors, and magnetic materials.

CHAPTER 2. COMPUTATIONAL METHODS

2.1 Structure Modeling

Structural models of pure ZnO and Mn-doped ZnO were constructed to investigate the material's properties. The pure ZnO system was simulated as a basic 1×1×1 unit cell (4 atoms), while the Mn-doped ZnO system was constructed as a 2×2×1 supercell (16 atoms) to accommodate dopant atoms and minimize artificial periodic interactions. In the Mn-doped model, one Zn atom was replaced with Mn, resulting in a doping concentration of 12.5%. These models (Figure 2.1) serve as the basis for further first-principles calculations[44].

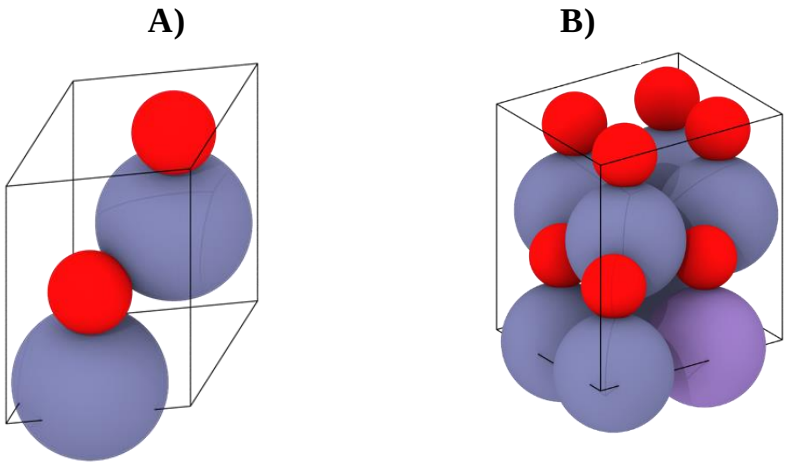

Figure 2.1 Atomic structures of ZnO. (A) Simple ZnO unit cell, where red spheres represent oxygen atoms and blue spheres represent zinc atoms. (B) Mn-doped ZnO structure (12.5% Mn) corresponding to a 2×2×1 supercell with 16 atoms in total: 7 Zn, 8 O, and 1 Mn. The red spheres denote oxygen atoms, blue spheres zinc atoms, and the purple sphere marks the manganese dopant.

To investigate the influence of Mn doping on the structural, electronic, and magnetic properties of ZnO, we constructed and optimized several bulk and surface models. For the bulk phase, three supercells derived from the primitive ZnO wurtzite structure were used (Figure 2.2): 2×2×2 (32 atoms), 3×3×1 (36 atoms), and 4×2×1 (32 atoms). In every scenario, one Zn atom was substituted by a Mn atom, corresponding to doping levels between 5.55% and 6.25%. These structures were visualized using OVITO and served as the basis for spin-polarized DFT calculations.

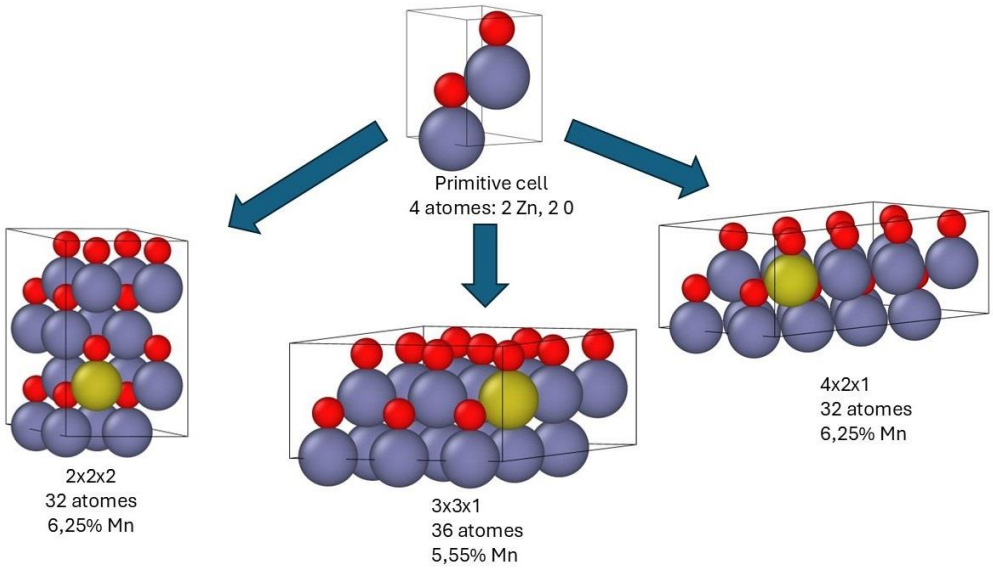

Figure 2.2 Schematic of Mn-doped ZnO supercells. Zn atoms are shown in purple, O atoms in red, and the substituted Mn atom is highlighted in green.

To extend this investigation to surface effects, slab models of Mn-doped ZnO were were produced and optimised to assess the influence of dopant placement on structural stability and electronic properties. Motivated by the technique of Liang et al.[45], a 3×2×1 supercell was cleaved along the non-polar $(10\bar{1}0)$surface using a Python script (Figure 2.3). The resulting slabs consisted of five atomic layers and included a vacuum spacing of 15 Å (7.5 Å on each side) along the z-direction to prevent periodic image interactions. To study site-specific substitutional effects, Mn atoms were manually placed at six inequivalent Zn sites (indexed 0 to 5) using OVITO[46].

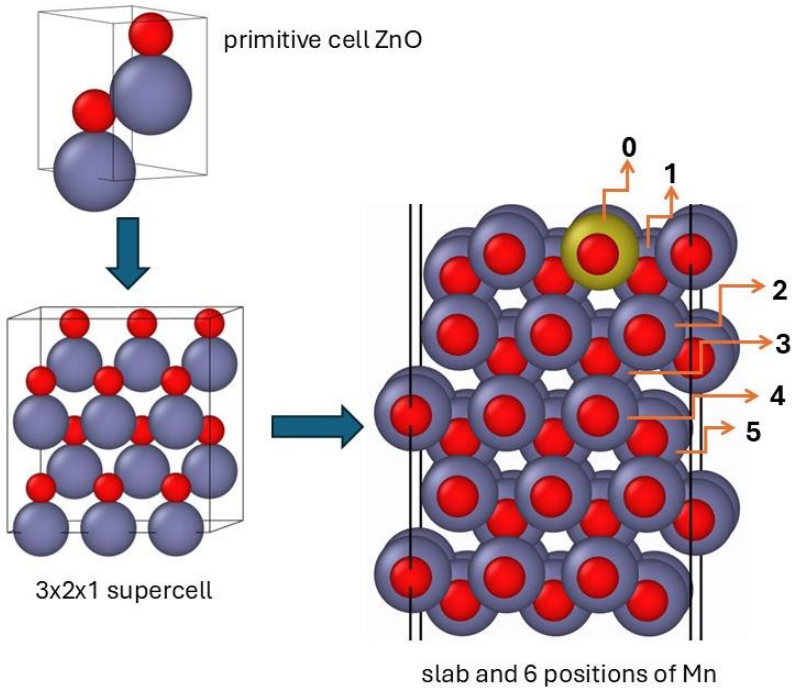

Figure 2.3 Construction of Mn-doped ZnO surface slab models and substitution positions for Mn at six inequivalent Zn sites.

2.2 Computational Details

All calculations were performed using the Vienna *Ab initio* Simulation Package (VASP)[47-50], implementing density functional theory (DFT) within the projector augmented-wave (PAW) method. The interaction between valence electrons and ionic cores was treated with PAW pseudopotentials, and a plane-wave basis set was used to expand valence wavefunctions. Exchange–correlation effects were treated using both the PBE functional under the generalized gradient approximation (GGA) and the optPBE-vdW functional, which incorporates non-local van der Waals interactions. To address the well-known underestimation of band gaps in conventional DFT, the DFT+U approach was employed using Dudarev's formalism (LDAUTYPE = 2), applying effective on-site Coulomb interactions of 4.0 eV for Zn 3d orbitals and 2.0 eV for Mn 3d orbitals. For selected structures, the PBE0 hybrid functional, incorporating 25% exact Hartree–Fock exchange, was used to benchmark the electronic structure, particularly the band gap. All geometry optimizations were carried out using the quasi-Newton algorithm (IBRION = 1), with force convergence criteria of 0.01 eV/Å for bulk and 0.05 eV/Å for hybrid calculations, and electronic self-consistency thresholds set to 10^{-6} or 10^{-7} eV depending

on the step. A high plane-wave cutoff energy of 650 eV was used during relaxations to reduce Pulay stress, while single-point energy and DOS calculations were performed at 500 eV. Monkhorst–Pack k-point grids were automatically generated with a spacing of 0.35 $Å^{-1}$ and set to Γ-centered meshes (KGAMMA = TRUE), ensuring proper Brillouin zone sampling. Spin polarization was explicitly considered in all simulations (ISPIN = 2), and the magnetic moment of Mn was initialized to 5 μB (MAGMOM), consistent with the high-spin d^5 configuration. For accurate density of states (DOS) and projected DOS (PDOS) analysis, the tetrahedron method with Blöchl corrections (ISMEAR = -5) was used, employing a dense energy grid (NEDOS = 3001) and enabling orbital-resolved outputs (LORBIT = 11). The van der Waals interactions were included via LUSE_VDW = .TRUE., and symmetry was preserved throughout the relaxations. All calculations were performed using high precision (PREC = Accurate) and non-spherical contributions to PAW spheres were included (LASPH = .TRUE.). This comprehensive computational framework allowed for the systematic study of how Mn doping and its spatial location affect the structural, magnetic, and electronic properties of both bulk and slab ZnO systems, and served as the foundation for further development of machine-learned interatomic potentials.

CHAPTER 3. RESULTS AND DISCUSSION

3.1 Convergence Tests

Pure ZnO system

In DFT calculations, convergence testing is a crucial step to ensure the reliability and accuracy of the results. Key parameters such as the plane-wave cutoff energy (ENCUT) and k-point sampling must be systematically tested. For ENCUT, the total energy of the system is monitored over a range of values to identify the point at which increasing the cutoff no longer significantly improves the accuracy, thereby ensuring computational efficiency. Similarly, k-point convergence testing involves varying the density of the k-point mesh to achieve an adequate sampling of the Brillouin zone. These tests provide a robust framework for selecting computational parameters that balance accuracy and computational cost, ensuring the reliability of DFT calculations across a wide range of materials. To ensure the accuracy and reliability of DFT calculations, systematic convergence tests were performed for the plane-wave cutoff energy (ENCUT) and k-point sampling (KSPACING) on the pristine ZnO system (Figure 3.1). The plane-wave cutoff energy was systematically varied from 300 eV to 1000 eV in increments of 50 eV. At lower cutoff values (300–400 eV), the total energy per atom exhibited significant fluctuations, indicating poor numerical convergence. Stabilization was achieved for ENCUT $\geq$ 500 eV, with energy variations below 0.001 eV/atom for higher cutoff values. Beyond 600 eV, further increases in ENCUT yielded negligible improvements in accuracy but resulted in significantly higher computational costs. Based on these results, an optimal cutoff energy of 500 eV was selected to balance numerical accuracy and computational efficiency. The impact of k-point sampling on energy convergence was examined by varying the k-point spacing (KSPACING) between 0.10 $Å^{-1}$ and 0.70 $Å^{-1}$. The total energy per atom remained stable for KSPACING $\leq$ 0.35, with minimal variations ($\sim$0.00025 eV/atom) and the lowest energy observed at KSPACING = 0.10 $Å^{-1}$. For KSPACING > 0.40, the energy began to deviate significantly, indicating insufficient sampling of the Brillouin zone. Consequently, a KSPACING value of 0.35 $Å^{-1}$ was selected as a practical choice, offering a balance between energy accuracy and computational cost.

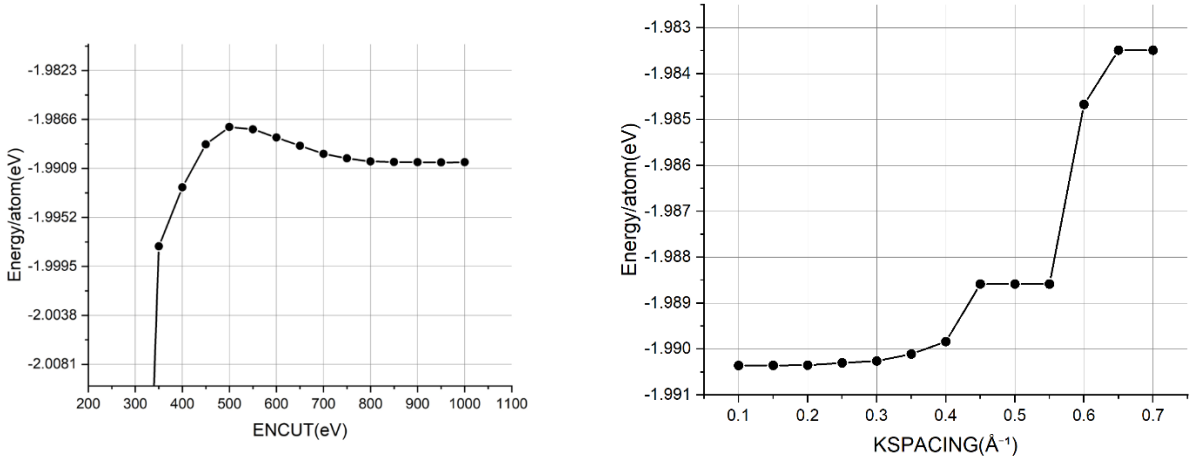

Figure 3.1 Convergence of the total energy per atom for the pure ZnO system as a function of (left) plane-wave cutoff energy (ENCUT) and (right) k-point sampling density (KSPACING). The total energy stabilizes beyond ENCUT = 500 eV and KSPACING = 0.35 $Å^{-1}$, indicating suitable values for DFT calculations.

The role of structural optimization in DFT calculations was investigated by comparing the convergence behavior of the total energy concerning ENCUT for optimized and non-optimized ZnO structures. Structural optimization, involving iterative relaxation of atomic positions and lattice parameters, was performed to minimize forces on the atoms and achieve an energetically favorable configuration. The results indicate that the optimized structure consistently exhibited lower energy per atom across all ENCUT values compared to the non-optimized counterpart, reflecting the effectiveness of structural relaxation in capturing the material's ground-state configuration. For non-optimized structures, higher energy values were observed, as expected, though the convergence behaviour can be seen to be very similar (Figure 3.2). The optimized structure ensures a reliable basis for subsequent electronic structure calculations, enabling accurate predictions of material properties.

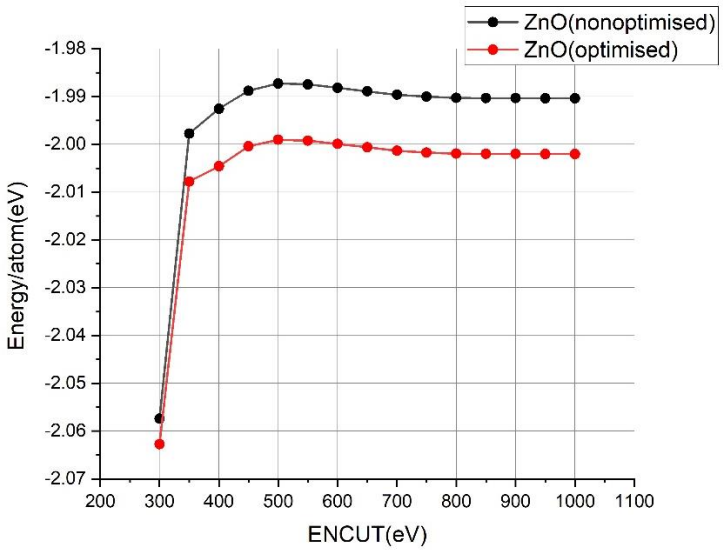

Figure 3.2 Comparison of total energy per atom for optimized and non-optimized ZnO structures across various ENCUT values.

Mn-Doped ZnO System

The convergence tests for Mn-doped ZnO focused on determining the optimal computational parameters for reliable and efficient DFT calculations (Figure 3.3). Both the plane-wave cutoff energy (ENCUT) and k-point spacing (KSPACING) were systematically tested under spin-polarized (ISPIN=2) and non-spin-polarized (ISPIN=1) conditions. The inclusion of spin polarization was particularly critical for systems doped with transition metals like Mn due to the localized nature of their d-electrons and associated magnetic interactions. An additional test utilizing the updated Mn partial valence pseudopotential (PAW PBE, 13 valence electrons) improved the description of Mn's d-electrons and revealed the necessity for higher ENCUT values due to the increased accuracy. The dynamic scaling of ENCUT during structural relaxation ensured consistency in total energy and force calculations, particularly for spin-polarized systems. These findings underscore the importance of careful parameter selection and pseudopotential accuracy when studying transition metal-doped systems. The ENCUT tests revealed stabilization of total energy at 600 eV for non-spin-polarized calculations, while spin-polarized configurations required at least 800 eV to resolve spin-split states accurately. Similarly, the KSPACING convergence tests demonstrated stabilization of energy at values ≤ 0.30 Å^{-1}, with significant deviations observed for KSPACING > 0.45 Å^{-1}. These results align with prior studies highlighting the importance of dense k-point grids for systems with defects and dopants. An additional test utilizing the updated Mn

pseudopotential (PAW PBE, 13 valence electrons) improved the description of Mn's d-electrons and revealed the necessity for higher ENCUT values due to the increased accuracy. The dynamic scaling of ENCUT during structural relaxation ensured consistency in total energy and force calculations, particularly for spin-polarized systems.

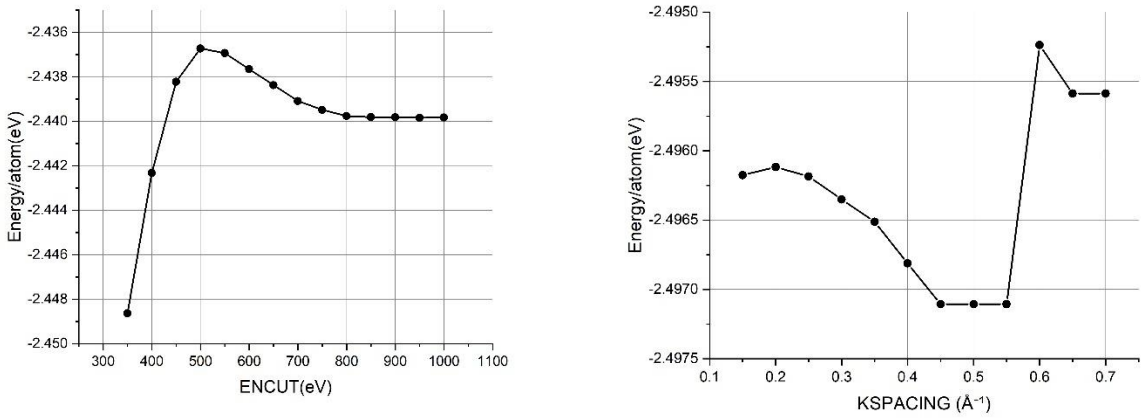

Figure 3.3 Convergence tests for the Mn-doped ZnO system. Total energy per atom as a function of (left) plane-wave cutoff energy (ENCUT) and (right) k-point sampling density (KSPACING). The energy converges beyond ENCUT = 500 eV and KSPACING = 0.35 $Å^{-1}$, indicating appropriate convergence parameters for subsequent DFT calculations.

3.2 Lattice Parameter Analysis

Pure ZnO system

The pure ZnO system, modeled as a fundamental 1×1×1 unit cell, was fully relaxed. The lattice constants were determined as a = 3.2898 Å, b = 3.2898 Å, and c = 5.3193 Å, with a unit cell volume of 49.857 $Å^3$ and a c/a ratio of 1.617. These values are roughly consistent with experimental and computational references, confirming the reliability of the computational setup[50]. Results presented in Table 3.2.

Table 3.2 Geometrical parameters of pure ZnO

Parameter	Experiment	optPBE-vdW	HSE06	HSE06 (0.375HFX)	PBE0
a (Å)	3.250	3.290	3.259	3.247	3.257
b (Å)	3.250	3.290	3.259	3.247	3.257
c (Å)	5.207	5.319	5.237	5.208	5.235

Cell Volume (Å³)	47.630	49.857	48.172	47.562	48.082
c/a Ratio	1.602	1.617	1.607	1.604	1.608
Angles (°)	α = 90°, β = 90°, γ = 120°				

Mn-Doped ZnO System

The Mn-doped ZnO system was modeled as a 2×2×1 supercell. Structural relaxation revealed slight lattice expansion compared to pure ZnO, with a = 3.2983 Å, b = 3.2983 Å, and c = 5.3410 Å. The unit cell volume increased to 50.319 $Å^3$, and the c/a ratio was 1.619. These changes, while subtle, reflect the localized electronic effects induced by Mn doping. The Mn–O bond length was consistently measured at 2.064˚A across computational methods, with the wurtzite symmetry preserved. Results presented in Table 3.3.

Table 3.3 Geometrical parameters of Mn-doped ZnO for different computational methods

Parameter	optPBE-vdW	HSE06	HSE06 (0.375HFX)	PBE0
a (Å)	3.298	3.2745	3.265	3.2725
b (Å)	3.298	3.2745	3.265	3.2725
c (Å)	5.341	5.251	5.228	5.254
Cell Volume (Å³)	50.319			
c/a Ratio	1.619	1.604	1.601	1.606
Mn–O Dist. (Å)	2.064	2.064	2.064	2.063
Angles (°)	α = 90°, β = 90°, γ = 120°			

Figure 3.4 presents a detailed analysis of the structural parameters for Mn-doped ZnO systems as a function of U(Zn) and U(Mn) values. The examined parameters include the lattice constants a and c, their ratio c/a, and the distance between Mn and the nearest oxygen atom. Dashed lines in the plots indicate reference values obtained from hybrid functional calculations using HSE06, HSE06 (0.375 HF exchange), and PBE0. The lattice constant a, as shown in the top panel, exhibits minor fluctuations across different U(Zn) and U(Mn) combinations, stabilizing near the reference values predicted by hybrid functional calculations. This observation indicates that Ueff has a minimal effect on the axis, maintaining the hexagonal symmetry of the ZnO lattice. The second panel highlights the c-direction lattice constant, which demonstrates a more pronounced

dependence on U, particularly for larger U(Zn) values. A gradual reduction in c is observed as U(Mn) increases, reflecting the structural adjustments associated with stronger electronic correlations within Mn d-orbitals. The third panel shows the ratio a/c, an indicator of the anisotropy of the ZnO lattice. The results display subtle variations in c/a across the tested parameter space, yet the ratio remains close to the reference values provided by HSE06 and PBE0. This consistency underscores the robustness of the wurtzite structure under varying Coulomb correction parameters. Finally, the bottom panel depicts the distance between Mn and the nearest oxygen atom (Mn–O bond length) as a function of U(Zn) and U(Mn). The Mn–O bond length shows a strong sensitivity to U(Mn), with larger values of U(Mn) resulting in slight elongations of the bond. This behavior is consistent with increased localization of Mn d-states due to the on-site Coulomb correction. The results indicate that the lattice parameters and Mn–O bond length are subtly influenced by the choice of U. Despite these variations, the structural parameters remain consistent with the experimentally observed wurtzite phase of ZnO, demonstrating that Mn doping and Hubbard corrections preserve the crystal symmetry while introducing minor distortions.

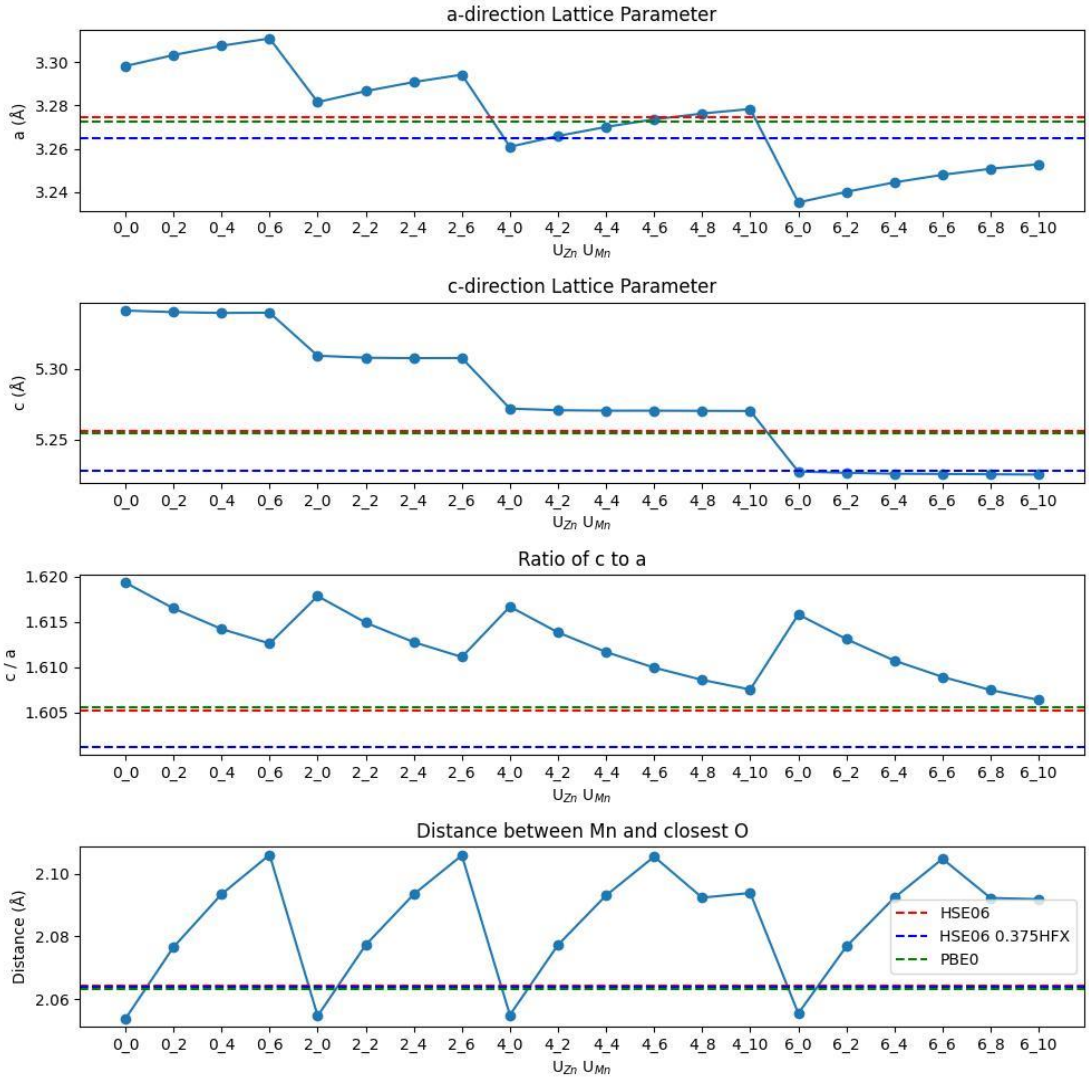

Figure 3.4 Lattice parameter analysis for Mn-doped ZnO. The plots display the lattice parameters a and c, their ratio c/a, and the distance between Mn and the closest O atom for different values of U(Zn) – U(Mn). Lines with dashes reflect values for comparison from HSE06, HSE06 (0.375 HF exchange), and PBE0 functionals.

3.3 Density of States (DOS)

Pure ZnO system

The calculated element-resolved and orbital-projected density of states (PDOS) for ZnO in a hexagonal structure, as derived from the CONTCAR file, is presented in Figures 3.5 and 3.6. The contributions from Zn d-orbitals and O p-orbitals are analyzed alongside the total density of states (TDOS). The Fermi level is aligned at 0 eV for reference, indicated by a dashed vertical line in the figure. A notable feature is the strong hybridization between the Zn d-orbitals and O p-orbitals, observed in the energy range of

approximately −6 eV to −4 eV, which signifies significant bonding interactions in this range. Above the Fermi level, the conduction band is dominated by contributions from Zn d-orbitals. IDOS for both spin-up and spin-down channels, computed up to the Fermi level, is analyzed. The IDOS curve provides insight into the cumulative number of electronic states available below a given energy. The spin-polarized calculation reveals no net spin polarization, consistent with the non-magnetic nature of ZnO. The rapid increase in IDOS near −5 eV corresponds to the high density of states within the valence band, dominated by contributions from O p-orbitals, further corroborating the orbital-resolved analysis.

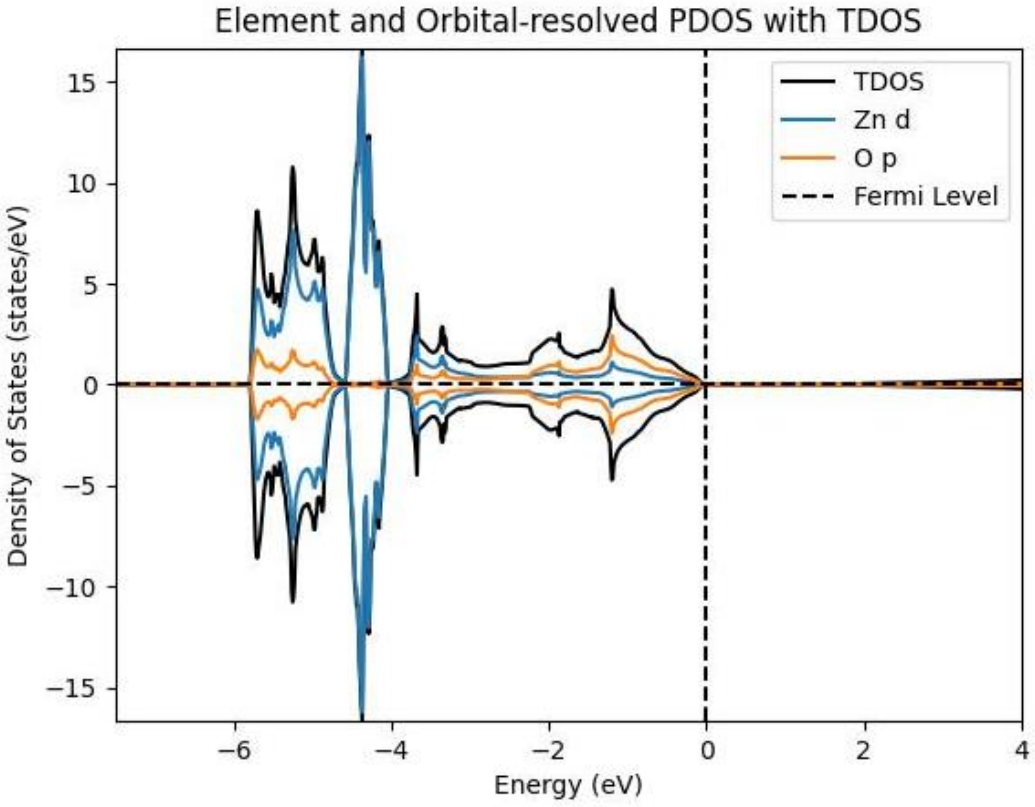

Figure 3.5 Element-resolved and orbital-projected PDOS with TDOS for ZnO.

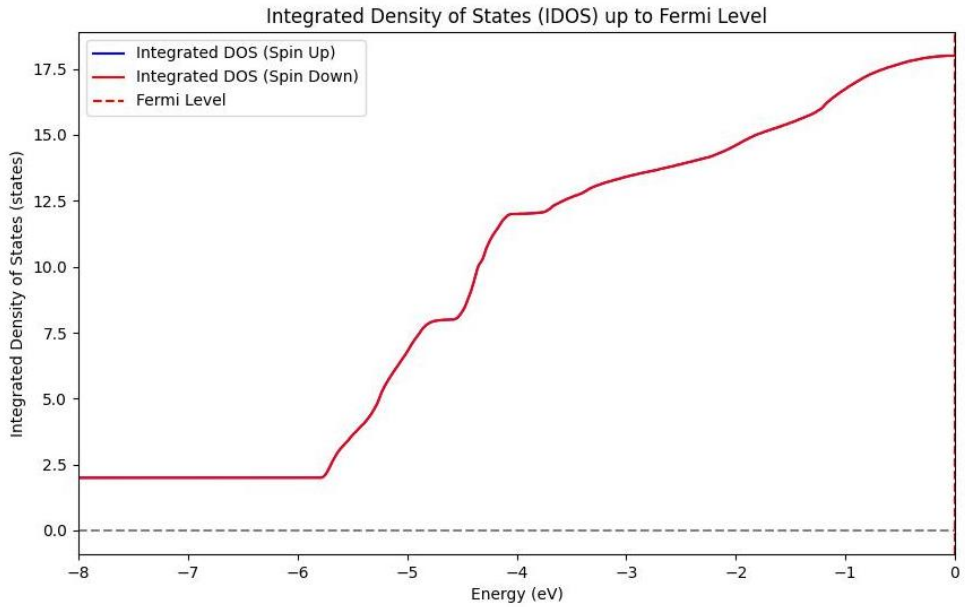

Figure 3.6 Integrated Density of States (IDOS) up to the Fermi level for ZnO.

The plot displays the cumulative density of electronic states for spin-down electrons (red curve), integrated from the lower energy levels up to the Fermi energy (marked by a dashed red line at 0 eV). The absence of the spin-up contribution suggests either spin degeneracy or negligible spin polarization in the considered system. The IDOS curve reveals distinct features corresponding to the valence band structure, providing insights into the electronic occupation up to the Fermi level.

Mn-Doped ZnO System

Spin-polarized DOS calculations for Mn-doped ZnO revealed localized Mn d-states within the band gap, contributing to spin polarization. Spin-resolved DOS showed distinct spin-up and spin-down channels, confirming the magnetic nature of the doped system. The Mn d-states also influenced the conduction band minimum, demonstrating the interplay between doping and electronic structure. The DFT+U method was applied to Mn-doped ZnO to account for strong electronic correlations in Mn d-states. Various combinations of U(Zn) and U(Mn) values were explored, ranging from 0 to 6 eV, resulting in 16 unique configurations. These configurations systematically revealed how Coulomb corrections influence the structural and electronic properties of Mn-doped ZnO.

Hybrid functional calculations using HSE06 and its modified variant (HSE06 with 37.5% Hartree–Fock exchange) further validated the results obtained from DFT+U.

The Hubbard U parameter effectively shifted the Mn d-states, introducing localized states within the band gap and enabling accurate modeling of magnetic and electronic properties. This adjustment highlighted the critical role of on-site Coulomb corrections in capturing the material's complex behavior.

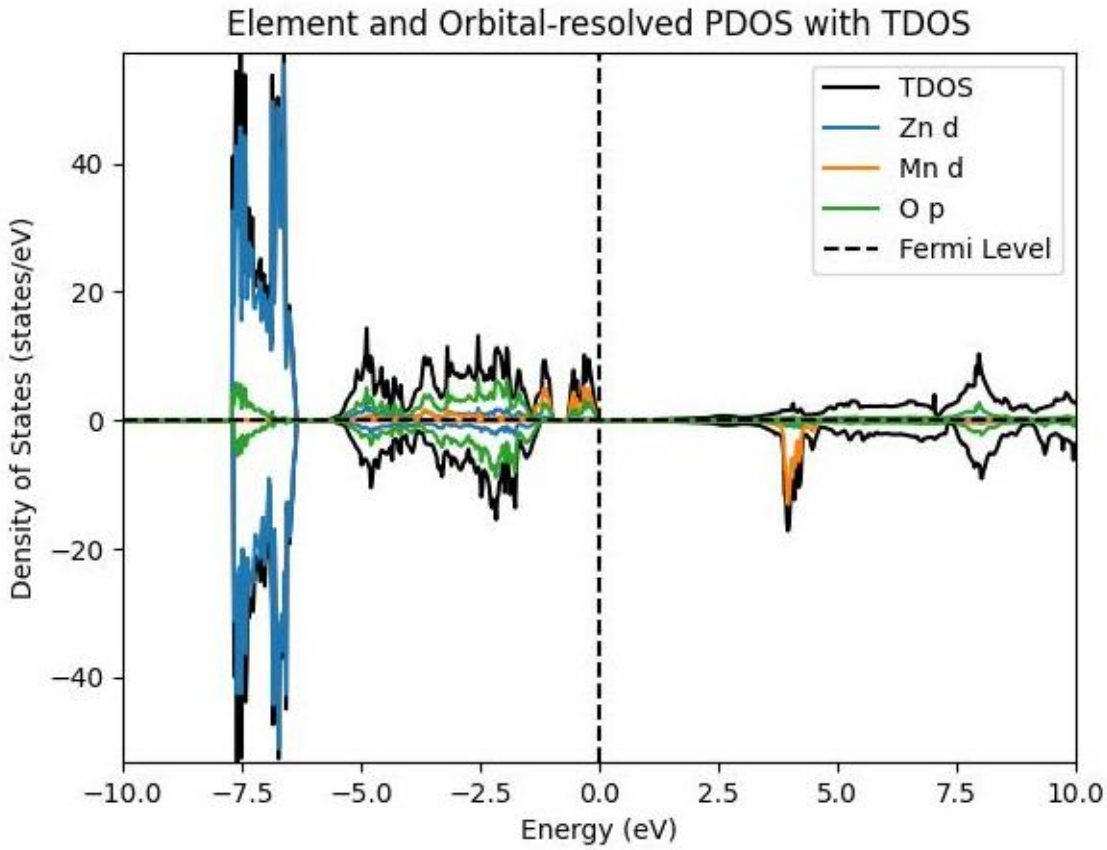

Figure 3.7 Element and orbital-resolved PDOS with TDOS for the U(Zn) = 4, U(Mn) = 2 configuration.

Figure 3.7 illustrates the projected density of states (PDOS) and total density of states (TDOS) for Mn-doped ZnO with U(Zn) = 4 eV and U(Mn) = 2 eV. This combination of Hubbard U-parameter was selected due to its close alignment with results from hybrid functional calculations, as demonstrated in Appendix A. The analysis sheds light on the electronic structure, hybridization, and the impact of Mn doping on the material's density of states. The TDOS, represented by the black curve, shows significant contributions from Zn d-orbitals in the valence band at around −7.5 eV, indicating their localized nature. The blue curve, corresponding to Zn d-orbitals, highlights their dominant role in shaping the electronic structure at these energies. Mn doping introduces

additional states near the Fermi level, as evidenced by the orange curve representing Mn d-orbitals. These states modify the electronic structure and contribute to spin polarization. Furthermore, the green curve, representing O p-orbitals, displays hybridization with both Zn d- and Mn d-orbitals, particularly in the valence band region. The Fermi level is positioned at 0 eV, marked by a dashed line, and a finite band gap of approximately 1.18 eV is observed. This value is consistent with hybrid functional calculations, as seen in the table in the Appendix A. The inclusion of Mn does not eliminate the band gap but introduces mid-gap states, which may influence the optical and magnetic properties of the material. The overlap between Mn d- and O p-orbitals is particularly notable, indicating strong hybridization that plays a critical role in the material's electronic and magnetic behavior. When compared with the pristine ZnO case shown in Figure A.2 in the Appendix A, it is evident that Mn doping significantly alters the density of states by introducing states near the Fermi level. Furthermore, as shown in Figure 1, the optPBE+U approach with U(Zn) = 4 eV and U(Mn) = 2 eV closely reproduces the trends observed in hybrid functional calculations, offering a computationally efficient yet accurate alternative.

Figure 3.8 and Table A.1 present a systematic investigation of how the choice of Hubbard U parameters for Zn and Mn within the DFT+U framework affects the electronic structure of Mn-doped ZnO. Based on the analysis of the minimum (Emin) and maximum (Emax) energies of the valence band — which reflect the depth and shape of the occupied states — the most accurate agreement with reference hybrid functional results (HSE06, HSE06 with 37.5% HF exchange, and PBE0) is achieved with the 4_2 configuration (U(Zn) = 4 eV , U(Mn) = 2 eV). At this point, the valence band edge positions are in closest alignment with hybrid-calculated benchmarks, indicating physically realistic localization of the valence electrons. While the widest band gap (1.41 eV) is observed for the configuration (U(Zn) =6 eV, U(Mn) = 10 eV), it is the 4_2 setting that provides the best overall balance between accurate valence band positioning and a reasonable, non-metallic band gap (0.33 eV). This suggests that 4_2 is the most physically justified configuration for DFT+U-based modeling of ZnO/Mn, especially when computational efficiency is prioritized over full band gap correction via hybrid functionals.

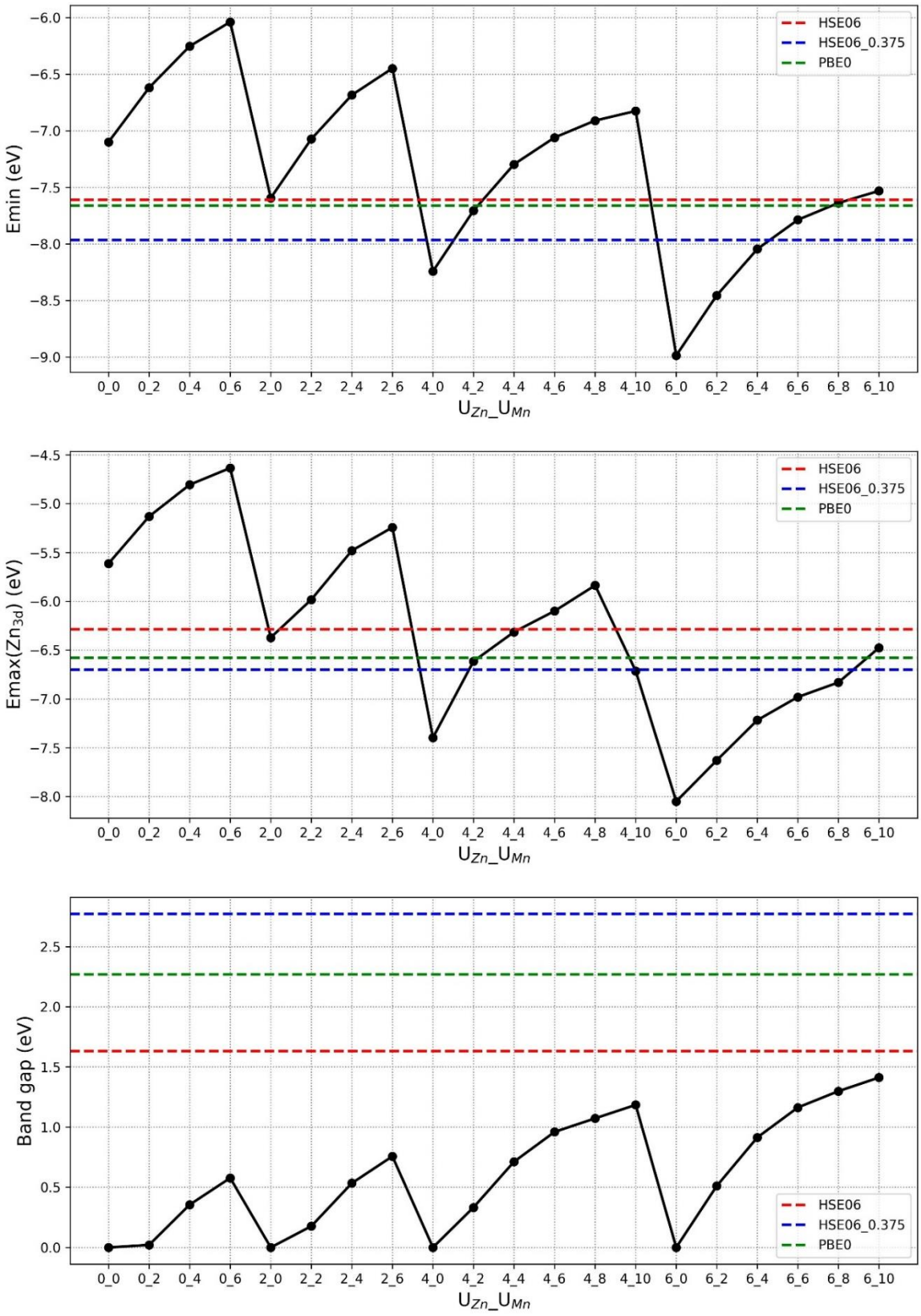

Figure 3.8 Analysis of density of states (DOS) for U(Zn) – U(Mn) configurations. The plots show the minimum energy (Emin), maximum energy (Emax), and the band gap as a function of U. Dashed lines correspond to reference values from HSE06, HSE06 (0.375 HF exchange), and PBE0 functionals.

3.4 Bulk Calculations

Three supercells based on the primitive cell ZnO structure were constructed to model Mn doping: a 2×2×2 supercell containing 32 atoms, a 3×3×1 supercell with 36 atoms, and a 4×2×1 supercell also with 32 atoms. In each case, one Zn atom was replaced with Mn, corresponding to a doping concentration of approximately 6 %. To examine magnetic effects, two types of spin initialization were tested: non-magnetic (all initial magnetic moments set to zero) and spin-polarized with a moment of 5 μB assigned to the Mn atom.

The exchange–correlation energy was treated using the optPBE-vdW functional, which includes van der Waals interactions via a nonlocal correlation term. The inclusion of van der Waals interactions is important for accurately describing water and oxide–water interactions, an important consideration for future studies of Mn-doped ZnO at the oxide–water interface. In addition to the optPBE-vdW calculations, two beyond-GGA approaches were used to treat the localized nature of Mn 3d electrons: the rotationally invariant DFT+U method and the PBE0 hybrid functional. The values of the effective Hubbard U parameters were set to 4.0 eV for Zn and 2.0 eV for Mn.

We first evaluated the electronic structure of the 2×2×2 supercell using the optPBE-vdW (hereafter referred to as optPBE) functional. Figure 3.9 presents the total and projected density of states (DOS) calculated with and without initialized spin polarization on Mn (i.e., MAGMOM = 0 vs. MAGMOM = 5 μB). It is evident that without initialized spin polarization, the calculation fails to reproduce the correct spin state, whereas initializing with MAGMOM = 5 μB yields a spin-aligned configuration corresponding to the lowest energy state. This results in noticeable changes in the DOS near the valence and conduction band edges.

In the top-left panel (optPBE without spin initialization), the Mn 3d states appear with contributions in both spin channels near the valence band edge. In contrast, in the top-right panel (optPBE with MAGMOM), only the spin-up channel is filled, while the spin-down states are unoccupied—consistent with a high-spin Mn(d^5) configuration. The zoomed-in panels at the bottom further highlight this contrast: in the spin-polarized case, the impurity peak in the majority-spin channel is sharp and well- localized, whereas in the non-magnetic case, this feature is delocalized. This observation confirms that without proper spin initialization, the system remains trapped in a metastable, low-spin

configuration, and fails to capture the mid-gap state critical for charge-transfer and catalytic activity. The emergence of the mid-gap state only in the spin-polarized calculation underscores the importance of explicitly setting the magnetic moment for transition metal dopants in DFT simulations. Similar trends were observed for the 3×3×1 and 4×2×1 supercells, as illustrated in Appendix A.

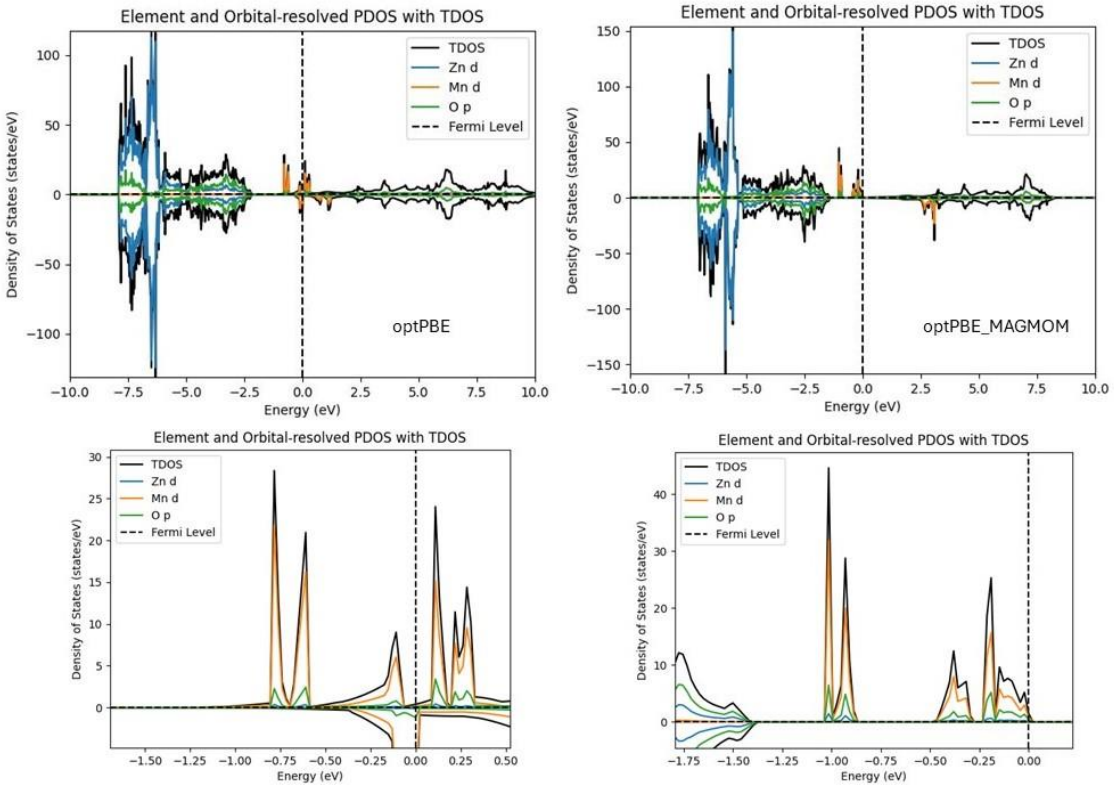

Figure 3.9 Element- and orbital-resolved partial density of states (PDOS) together with the total density of states (TDOS) for Mn- doped ZnO calculated using the optPBE functional. The left column shows results without initial magnetic moment initialization, while the right column corresponds to calculations with MAGMOM initialization. The bottom row presents zoomed-in views of the energy region near the Fermi level for each case.

To better describe the localized character of Mn 3d electrons, we carried out DFT+U calculations using the Dudarev approach with U(Mn) = 2 eV and U(Zn) = 4 eV. These trends highlight that while the Hubbard-U correction aids in reinforcing on-site electron localization, it cannot fully compensate for the absence of proper magnetic initialization when using cost-effective GGA-based functionals.

For further validation, the same 2×2×2 supercell was investigated using the PBE0 hybrid functional, which includes 25% exact non-local Hartree–Fock exchange. Figure

3.10 compares the DOS obtained from PBE0 with that from DFT+U for the same spin-polarized structure. Although the PBE0 calculation improves the overall band gap, the localization of Mn 3d states is less pronounced than in the DFT+U result. This suggests that the DFT+U method (with the chosen U values) provides a better qualitative description of the magnetic and electronic structure in Mn-doped ZnO than the hybrid functional for this particular case. The same trend was confirmed in the larger 3×3×1 and 4×2×1 supercells, where the DFT+U functional consistently produced more distinct separation between spin-up and spin-down states. The corresponding data and DOS plots are provided in the Appendix A.

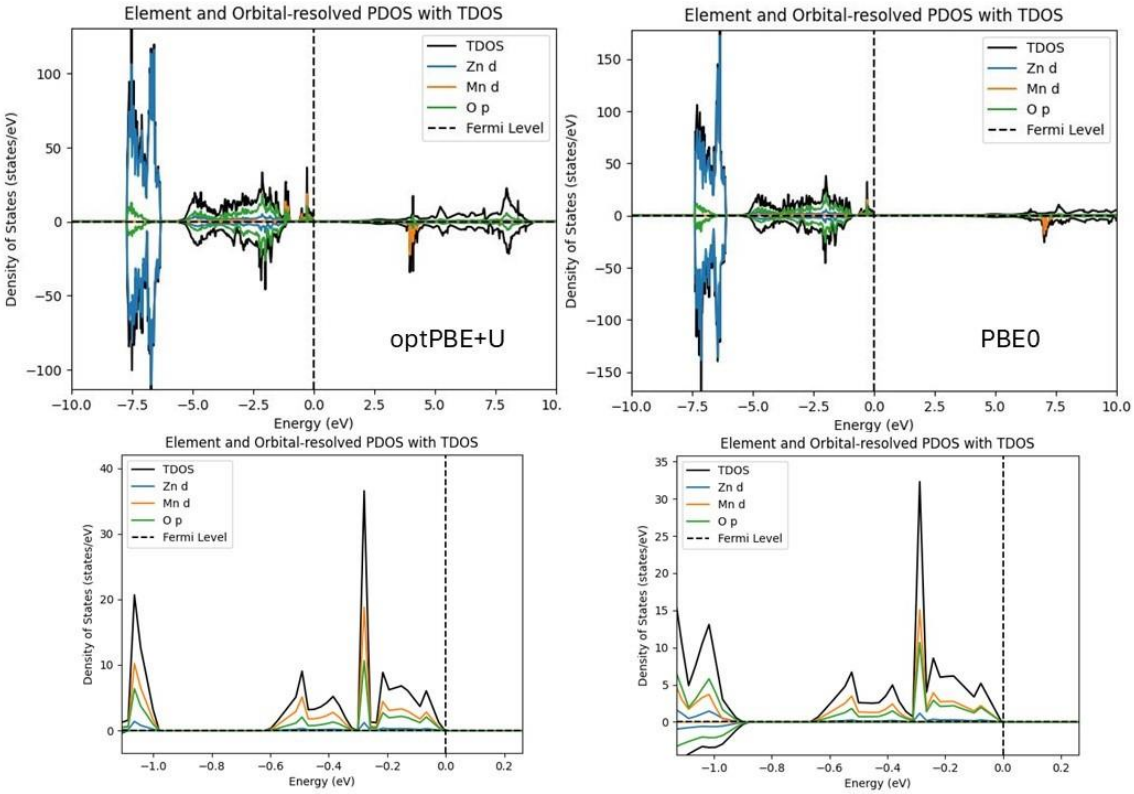

Figure 3.10 Element- and orbital-resolved partial density of states (PDOS) and total density of states (TDOS) for Mn-doped ZnO (2×2×2). Top: full-range spin-resolved PDOS obtained with the optPBE+U (left) and PBE0 (right) functionals. Bottom: zoomed-in views near the Fermi level (dashed line) for each case.

The influence of geometry on electronic structure was also examined. While minor distortions occurred around the Mn site due to size and electronic mismatch with Zn, the overall lattice parameters and local coordination remained close to those of ZnO.

3.5 Role of Initial Magnetic Moment Initialization (MAGMOM) in Spin-Polarized DFT Calculations of Mn-Doped ZnO

Proper initialization of local magnetic moments is essential for obtaining physically meaningful results in spin-polarized first-principles calculations of magnetic semiconductors. This is particularly critical when modeling open-shell 3d transition metal dopants such as Mn in wide-bandgap oxides like ZnO. Our results reveal a stark contrast between these two cases. Without spin initialization, the Mn site exhibits a significantly underestimated local magnetic moment (0.91 with optPBE), and the projected density of states (PDOS) shows Mn 3d states distributed across both spin channels near the valence band maximum, indicative of spin-degenerate behavior. Conversely, when initialized with MAGMOM = 5.0, the system converges to a magnetic ground state with a local moment of 4.3–4.5, depending on the functional, and a clearly split DOS consistent with a fully aligned high-spin configuration. Figure 3.11 summarizes the computed local moments on Mn under various conditions. Notably, the optPBE functional severely underestimates the spin polarization unless MAGMOM is defined, while optPBE+U and PBE0 yield robust magnetic solutions even in the absence of initialization, albeit with slightly reduced fidelity. These trends highlight that while the Hubbard-U correction serves a complementary function by enhancing on-site electron localization, it cannot fully replace the necessity for appropriate magnetic initialization when using cost-effective GGA-based functionals. Together, these findings stress that the MAGMOM tag is far more than a technical detail—it is a critical parameter for accurately capturing the spin-resolved electronic structure of ZnO/Mn systems.

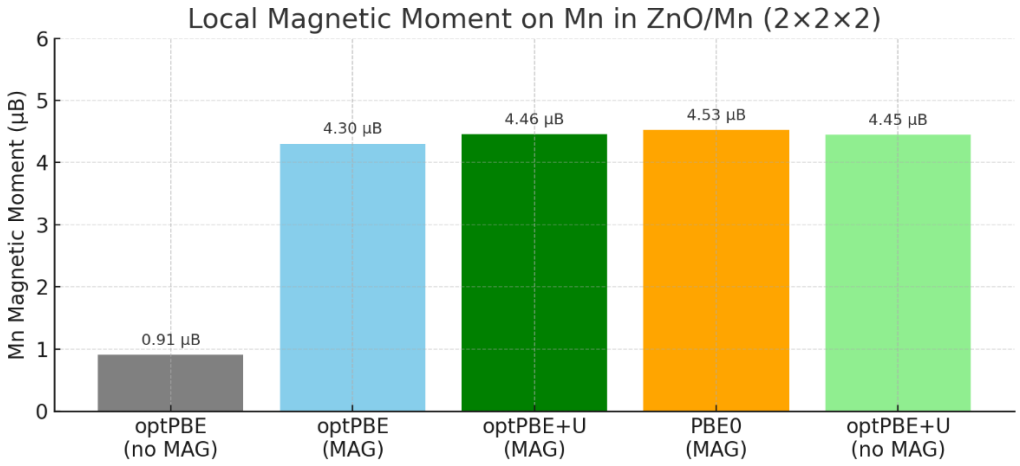

Figure 3.11 Local magnetic moment on Mn in ZnO/Mn (2×2×2 supercell) calculated using different functionals and magnetic initializations.

3.6 Slab Calculations

To investigate site-specific substitutional doping, we manually replaced Zn atoms with Mn at six inequivalent positions (indexed 0 to 5) using the OVITO visualization tool. This allowed us to probe the effects of dopant location, ranging from surface to subsurface regions, on the structural and magnetic properties.

Figure 3.12 presents the relative substitution energies for Mn at six inequivalent Zn sites within the ZnO surface slab, as computed using three different exchange-correlation approaches: optPBE, optPBE+U, and the PBE0 hybrid functional. All methods reveal a clear site dependence, but only optPBE+U and PBE0 consistently identify surface positions (site 0) as energetically favored. In particular, site 0 emerges as the most stable across all functionals, highlighting a thermodynamic preference for Mn incorporation on the surface rather than deeper subsurface layers.

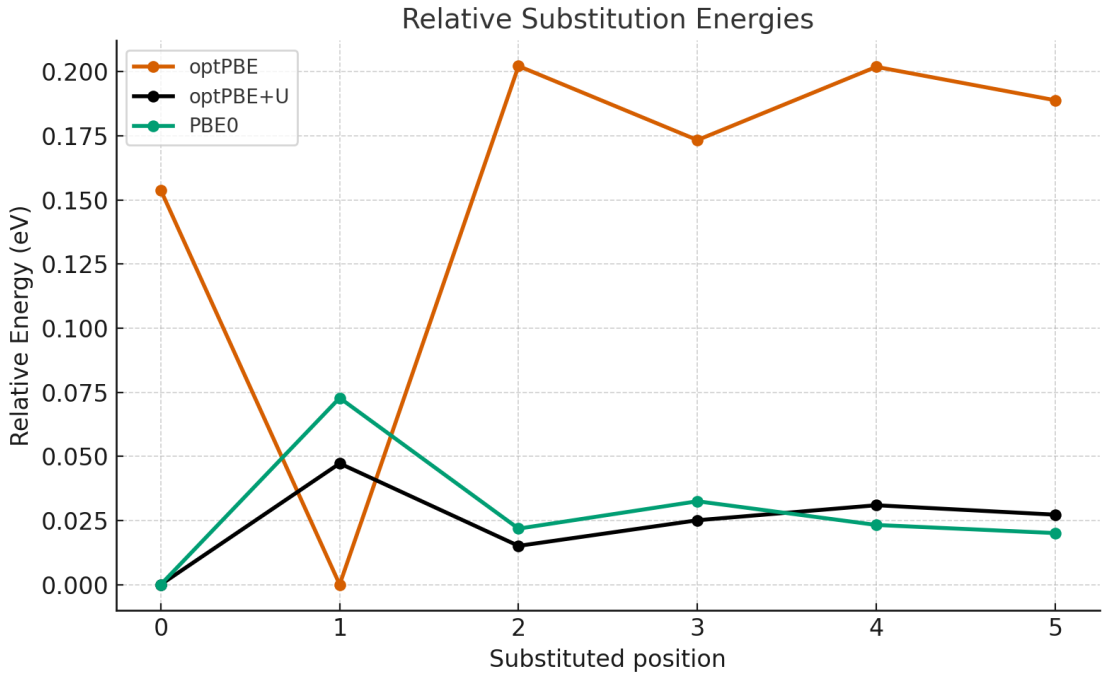

Figure 3.12 Relative substitution energies for Mn at six inequivalent Zn sites in the ZnO surface slab, calculated using optPBE, optPBE+U, and PBE0 functionals.

In contrast, the uncorrected GGA (optPBE) functional predicts a highly inconsistent energy profile, with artificially elevated substitution energies at most positions, underscoring its inadequacy in describing localized d-states. The improved consistency between optPBE+U and PBE0 not only validates the use of Hubbard-corrected GGA for modeling open-shell 3d dopants, but also strengthens the conclusion that Mn prefers surface incorporation. This energetic preference has direct implications for the design of Mn-functionalized ZnO surfaces, where surface-exposed dopants are more likely to participate in catalytic processes.

The strong agreement between optPBE+U and PBE0 confirms that Hubbard-U-augmented GGA can reproduce the essential physics of more expensive hybrid functionals. optPBE+U not only yields similar energetic trends but also provides a qualitatively correct picture of Mn incorporation with much lower computational cost. This validates its use in extensive slab and surface studies where computational feasibility is a constraint. Since dopants at the surface are more likely to interact directly with adsorbates and reaction intermediates, this finding has direct implications for catalyst design. Placing Mn at the surface could enhance redox activity, while subsurface configurations may offer electronic tuning without steric exposure. It serves as a computationally efficient alternative to hybrid functionals and supports the future development of machine learning potentials and large-scale simulations for ZnO.

CONCLUSIONS

1. Optimization of computational parameters (ENCUT, k-point mesh, spin initialization) was carried out for both pure and Mn-doped ZnO systems. The convergence tests resulted in optimal values of ENCUT = 500–800 eV and KSPACING = 0.3–0.35 $Å^{-1}$, ensuring a balance between accuracy and computational efficiency.
2. The optimal values of the Hubbard U parameters were determined by analyzing 16 different DFT+U configurations. The best agreement with hybrid functionals (PBE0, HSE06) was achieved using U(Zn) = 4.0 eV and U(Mn) = 2.0 eV, which reproduced key features of the density of states (DOS) with much lower computational cost.
3. DFT+U calculations were performed for various bulk ZnO supercells (2×2×2, 3×3×1, 4×2×1) doped with a single Mn atom. These models simulated different doping concentrations and preserved the wurtzite structure, with localized structural distortions near the Mn site.
4. Total and projected density of states (DOS/PDOS) were analyzed for both non-magnetic and spin-polarized configurations. The role of MAGMOM initialization was shown to be crucial for obtaining a physically correct high-spin configuration of Mn, avoiding convergence to metastable, non-magnetic states.
5. DFT+U results were compared with hybrid functionals (PBE0, HSE06) in terms of accuracy and computational cost. The DFT+U method closely reproduced the electronic structure predicted by hybrid functionals while being significantly more computationally efficient.
6. Slab models of the ZnO surface were constructed and relaxed, with Mn substituted at six inequivalent Zn positions. The substitution energies were calculated, showing strong site dependence and highlighting the importance of dopant location in surface stability.
7. The thermodynamically preferred dopant site was identified, with surface substitution (site 0) being the most favorable across all functionals. This result has direct implications for the catalytic activity of Mn-doped ZnO surfaces.

REFERENCES

1. Ringu T., Ghosh S., Das A., Pramanik N. Zinc oxide nanoparticles: An excellent biomaterial for bioengineering applications. *Emergent Mater.* **2022,** *5* 1629-1648.
2. Vyas S. A short review on properties and applications of zinc oxide-based thin films and devices: ZnO as a promising material for applications in electronics, optoelectronics, biomedical, and sensors. *Johnson Matthey Technol. Rev.* **2020,** *64* (2), 202-218.
3. Król A., Pomastowski P., Rafińska K., Railean-Plugaru V., Buszewski B. Zinc oxide nanoparticles: Synthesis, antiseptic activity and toxicity mechanism. *Adv. Colloid Interface Sci.* **2017,** *249* 37-52.
4. Chen Z., Wang J., Wu H., Yang J., Wang Y., Zhang J., Bao Q., Wang M., Zaifei, Tress W., Tang Z. A transparent electrode based on solution-processed ZnO for organic optoelectronic devices. *Nat. Commun.* **2022,** *13* 4387.
5. Kumar S., Rao K. Zinc oxide based photocatalysis: Tailoring surface-bulk structure and related interfacial charge carrier dynamics for better environmental applications. *RSC Adv.* **2015,** *5* 3306-3351.
6. Fakhari S., Jamzad M., Fard H. K. Green synthesis of zinc oxide nanoparticles: A comparison. *Green Chem. Lett. Rev.* **2019,** *12* 19-24.
7. Wojnarowicz J., Chudoba T., Lojkowski W. A review of microwave synthesis of zinc oxide nanomaterials: Reactants, process parameters and morphologies. *Nanomaterials* **2020,** *10(6)* 1086.
8. Xu H., Wang H., Zhang Y., He W., Zhu M., Wang B., Yan H. Hydrothermal synthesis of zinc oxide powders with controllable morphology. *Ceram. Int.* **2004,** *30* 93-97.
9. Musić S., Popović S., Maljković M., Dragčević Đ. Influence of synthesis procedure on the formation and properties of zinc oxide. *J. Alloys Compd.* **2002,** *347* 324-332.
10. Droepenu E., Wee B., Chin S., Kok K., Maligan M. F. Zinc oxide nanoparticles synthesis methods and its effect on morphology: A review. *Biointerface Res. Appl. Chem.* **2021**, *12(3)* 4261-4292.

11. Muiva C., Sathiaraj T., Maabong K. Effect of doping concentration on the properties of aluminium doped zinc oxide thin films prepared by spray pyrolysis for transparent electrode applications. *Ceram. Int.* **2011,** *37* 555-560.
12. Ali H., Jacob J., Khalid M., Mahmood K., Yusuf M., Mehboob K., Ikram S., Ali A., Amin N., Ashar A. Optimizing the structural, morphological and thermoelectric properties of zinc oxide by the modulation of cobalt doping concentration. *J. Alloys Compd.* **2021,** *871* 159564.
13. Kazmi J., Ooi P., Goh B. T., Lee M., Wee M. R., Karim S. S., Raza S. R. A., Mohamed M. Bi-doping improves the magnetic properties of zinc oxide nanowires. *RSC Adv.* **2020,** *10* 23297-23311.
14. Pratomo U., Fransisca N., Adzani M. D., Irkham, Sulaeman A., Eddy D. R., Mulyana J., Primadona I. Doping of rare earth element: The effects in elevated physical and optical properties of ZnO. *Talanta Open* **2025**, *11* 100411.
15. Noman M., Amor N., Petrů M. Synthesis and applications of ZnO nanostructures (ZONSs): A review. *Crit. Rev. Solid State Mater. Sci.* **2021,** *47* 99-141.
16. Mahmud A., Khan A., Voss P., Das T., Abdel-Rahman E., Ban D. A high-performance and consolidated piezoelectric energy harvester based on 1d/2d hybrid zinc oxide nanostructures. *Adv. Mater. Interfaces* **2018,** *5* 1801167.
17. Abubakar S., Tan S., Liew J., Talib Z., Sivasubramanian R., Vaithilingam C., Indira S., Oh W., Siburian R., Sagadevan S., Paiman S. Controlled growth of semiconducting ZnO nanorods for piezoelectric energy harvesting-based nanogenerators. *Nanomaterials* **2023,** *13(6)* 1025.
18. Güneri E., Henry J., Göde F., Özpozan N. Structural and optical properties of chemically deposited Mn-doped ZnO thin films. *J. Cent. South Univ.* **2023,** *30* 691-706.
19. Sharma D., Jha R. Transition metal (Co, Mn) co-doped ZnO nanoparticles: Effect on structural and optical properties. *J. Alloys Compd.* **2017,** *698* 532-538.
20. Ruilin L., Yee K. Y., Salleh N., Deghfel B., Zakaria Z., Yaakob M. K., Ong H., Rahiman W., Akbulut H., Wang D., Kheawhom S., Mohamad A. Hydrothermal synthesis of manganese doped zinc oxide wurtzite nanoparticles for supercapacitors – a brief review. *Inorg. Chem. Commun.* **2024,** *170(2)* 113311.

21. Liang Q., Brocks G., Sinha V., Bieberle-Hütter A. Tailoring the performance of ZnO for oxygen evolution by effective transition metal doping. *ChemSusChem* **2021**, *14* 3064 – 3073.
22. 23. Belkhaoui C., Mzabi N., Smaoui H. Investigations on structural, optical, and dielectric properties of mn Mn-doped ZnO nanoparticles synthesized by co-precipitation method. *Mater. Res. Bull.* **2019**, *111* 70-79.
23. Khan M. A., Kumar S., Alhazaa A., Al-Gawati M. Modifications in structural, morphological, optical and photocatalytic properties of ZnO: Mn nanoparticles by sol-gel protocol. *Mater. Sci. Semicond. Process.* **2018**, *87* 134-141.
24. Wang X., Luan C., Shao Q., Pruna A., Leung C., Lortz R., Zapien J., Ruotolo A. Effect of the magnetic order on the room-temperature band-gap of mn-doped zno thin films. *Appl. Phys. Lett.* **2013,** *102* 102112.
25. Shah W., Alam A., Javed H., Rashid K., Ali A., Ali L., Safeen A., Ali M., Imran N., Sohail M., Chambashi G. Tuning of the band gap and dielectric loss factor by Mn doping of Zn1-xMnO nanoparticles. *Sci. Rep.* **2023,** *13* 8646.
26. Sheikh M., Pazirofteh M., Dehghani M., Asghari M., Rezakazemi M., Valderrama C., Cortina J. Application of ZnO nanostructures in ceramic and polymeric membranes for water and wastewater technologies: A review. *Chem. Eng. J.* **2020,** *391* 123475.
27. Quaranta V., Hellström M., Behler J., Kullgren J., Mitev P., Hermansson K. Maximally resolved anharmonic OH vibrational spectrum of the water/ZnO ($10\bar{1}0$) interface from a high-dimensional neural network potential. *J. Chem. Phys.* **2018,** *148(24)* 241720.
28. Jafarova V., Orudzhev G. Structural and electronic properties of ZnO: A first-principles density-functional theory study within LDA (GGA) and LDA (GGA)+u methods. *Solid State Commun.* **2021,** *325* 114166.
29. Dudarev S. L., Botton G. A., Savrasov S. Y., Humphreys C. J., Sutton A. P. Electron-energy-loss spectra and the structural stability of nickel oxide: An lsda+u study. *Phys. Rev.B* **1998,** *57*(3), 1505-1509.
30. Vladimir I. A., Aryasetiawan F., Lichtenstein A. I. First-principles calculations of the electronic structure and spectra of strongly correlated systems: The lda+ u method. *J. Phys.: Condens. Matter* **1997,** *9*(4) 767.

31. Mandal S., Haule K., Rabe K., Vanderbilt D. Systematic beyond-dft study of binary transition metal oxides. *npj Comput. Mater.* **2019,** *5* 115.
32. Tolba S., Gameel K., Ali B., A.Almossalami H., Allam N. The dft+u: Approaches, accuracy, and applications. *Density Functional Calculations - Recent Progresses of Theory and Application* **2018**.
33. Greiner W. The schrödinger equation. In *Quantum mechanics: An introduction*, Greiner, W., Ed. Springer Berlin Heidelberg: Berlin, Heidelberg, **2001**; pp 117-155.
34. Atkins P., Friedman R. *Molecular quantum mechanics*. 5 ed.; Oxford University Press: Oxford, **2011**.
35. Hohenberg P., Kohn W. Inhomogeneous electron gas. *Phys. Rev.* **1964,** *136* (3B), B864-B871.
36. Kohn W., Sham L. J. Self-consistent equations including exchange and correlation effects. *Phys. Rev.* **1965,** *140* (4A), A1133-A1138.
37. Parr R. G., Yang W. *Density-functional theory of atoms and molecules*. Oxford University Press: New York, **1989**.
38. Perdew J. P., Burke K., Ernzerhof M. Generalized gradient approximation made simple. *Phys. Rev. Lett.* **1996,** *77* (18) 3865-3868.
39. Perdew J. P., Ruzsinszky A., Csonka G. I., Vydrov O. A., Scuseria G. E., Constantin L. A., Zhou X., Burke K. Restoring the density-gradient expansion for exchange in solids and surfaces. *Phys. Rev. Lett.* **2008,** *100* 136406.
40. Cococcioni M., de Gironcoli S. Linear response approach to the calculation of the effective interaction parameters in the $\mathrm{lda}+\mathrm{u}$ method. *Phys. Rev. B* **2005,** *71* (3), 035105.
41. Blöchl P. E. Projector augmented-wave method. *Phys. Rev. B* **1994,** *50* (24), 17953–17979.
42. Kresse G., Joubert D. From ultrasoft pseudopotentials to the projector augmented-wave method. *Phys. Rev. B* **1999,** *59* 1758–1775.
43. Cao H., Lu P., Cai N., Zhang X., Yu Z., Gao T., Wang S. First-principles study on electronic and magnetic properties of (mn,fe)-codoped zno. *J. Magn. Magn. Mater.* **2014,** *352* 66-71.
44. Liang Y., Hu C., Huo Z., Hu L., Luo W. Mn-doped ZnO with rich oxygen vacancies for enhanced oxygen evolution reaction. **2021,** *14* (14), 3081–3088.

45. Stukowski A. Visualization and analysis of atomistic simulation data with ovito–the open visualization tool. *Modelling Simul. Mater. Sci. Eng.* **2010,** *18* (1), 015012.
46. Kresse G., Furthmüller J. Efficiency of ab-initio total energy calculations for metals and semiconductors using a plane-wave basis set. *Comput. Mater. Sci.* **1996,** *6* 15–50.
47. Kresse G., Furthmüller J. Efficient iterative schemes for ab initio total-energy calculations using a plane-wave basis set. *Phys. Rev. B* **1996,** *54* 11169–11186.
48. Kresse G., Hafner J. Ab initio molecular dynamics for liquid metals. *Phys. Rev. B* **1993,** *47* 558.
49. Kresse G., Hafner J. Ab initio molecular-dynamics simulation of the liquid-metal–amorphous-semiconductor transition in germanium. *Phys. Rev. B* **1994,** *49* 14251.
50. Özgür Ü., Alivov Y. I., Liu C., Teke A., Reshchikov M. A., Doğan S., Avrutin V., Cho S.-J., Morkoç H. Zinc oxide—from synthesis to application: A review. *J. Appl. Phys.* **2007,** *120* (1–3), 40–49.

APPENDIX A

Table A.1 Energy levels and band gap data for U(Zn) – U(Mn) combinations on DOS and reference values from HSE06, HSE06 (0.375 HF exchange), and PBE0

U(Zn) - U(Mn)	E min (eV)	E max (eV)	Band Gap (eV)
0.0	-7.099	-5.613	0.0
0.2	-6.618930	-5.131	0.02077
0.4	-6.252	-4.806	0.355
0.6	-6.038	-4.6348	0.577
2.0	-7.5936	-6.372	0.0
2.2	-7.0727	-5.983	0.176532
2.4	-6.6836	-5.4808	0.534
2.6	-6.4478	-5.2432	0.757
4.0	-8.242	-7.397	0.0
4.2	-7.706	-6.6153	0.3326
4.4	-7.296	-6.3146	0.7124
4.6	-7.0593	-6.0999	0.9598
4.8	-6.9097	-5.8372	1.0725
4.10	-6.825	-6.7136	1.184388
6.0	-8.986	-8.0509	0.0
6.2	-8.455	-7.6297	0.511
6.4	-8.0455	-7.218	0.914
6.6	-7.7870	-6.981	1.16278
6.8	-7.638	-6.8316	1.29828
6.10	-7.53128	-6.477	1.411308
HSE06 (ref)	-7.61	-6.2856	1.6313
HSE06 (0.375 HF)	-7.967	-6.70149	2.77
PBE0 (ref)	-7.6595	-6.58009	2.268

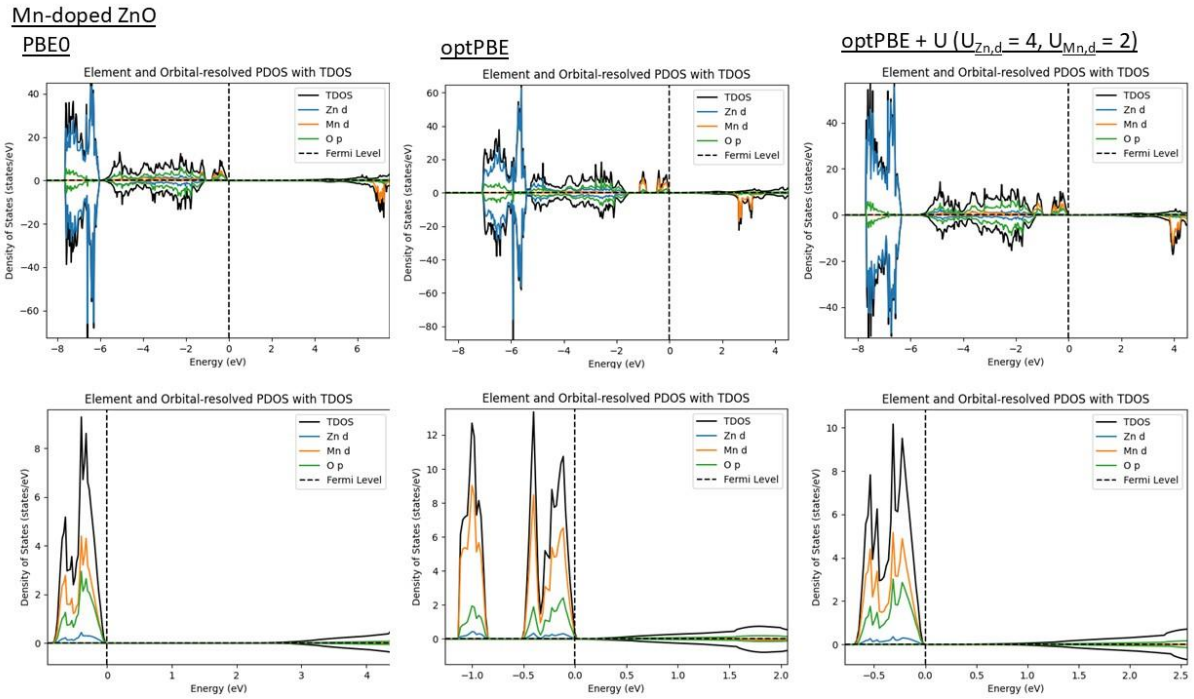

Figure A.1 Electronic structure analysis of Mn-doped ZnO using different computational methods: PBE0, optPBE, and optPBE + U (UZn-d = 4, UMn-d = 2). Each column represents the TDOS and PDOS for Zn d, Mn d, and O p orbitals under the corresponding functionals.

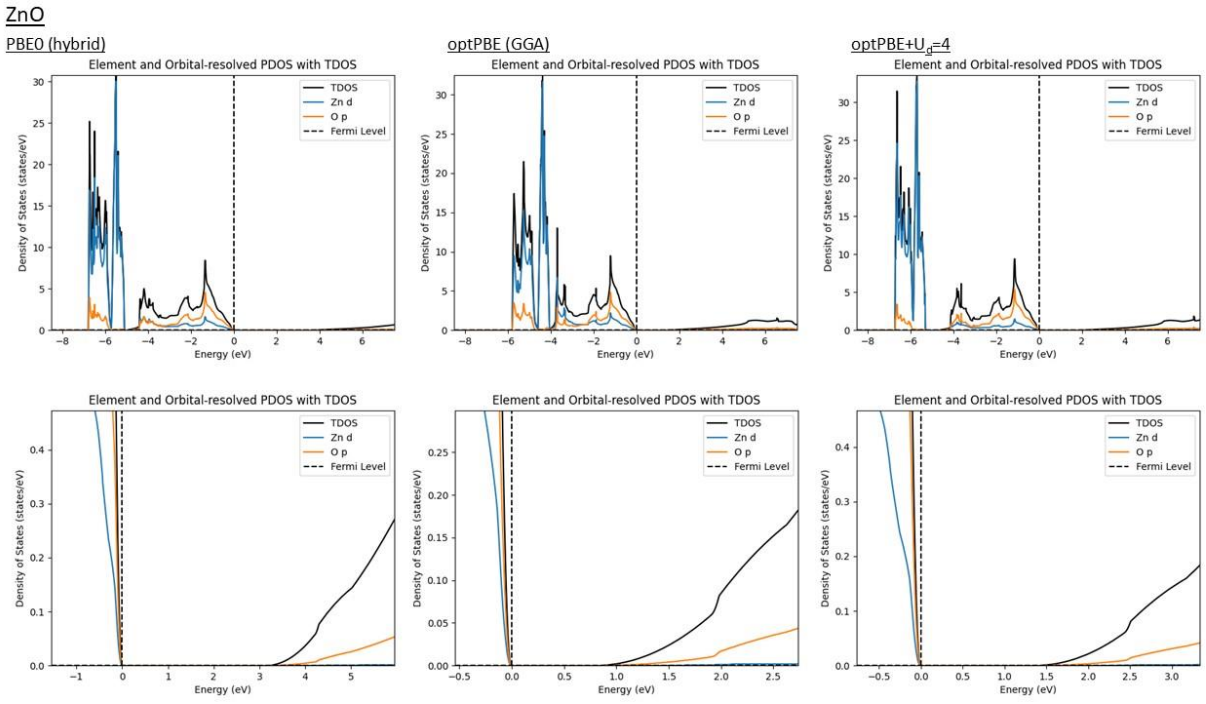

Figure A.2 Electronic structure analysis of pristine ZnO using different computational methods: PBE0 (hybrid), optPBE (GGA), and optPBE + U (UZn-d = 4). Each column represents the TDOS and PDOS for Zn d and O p orbitals under the corresponding functionals. The Fermi level is set at 0 eV.

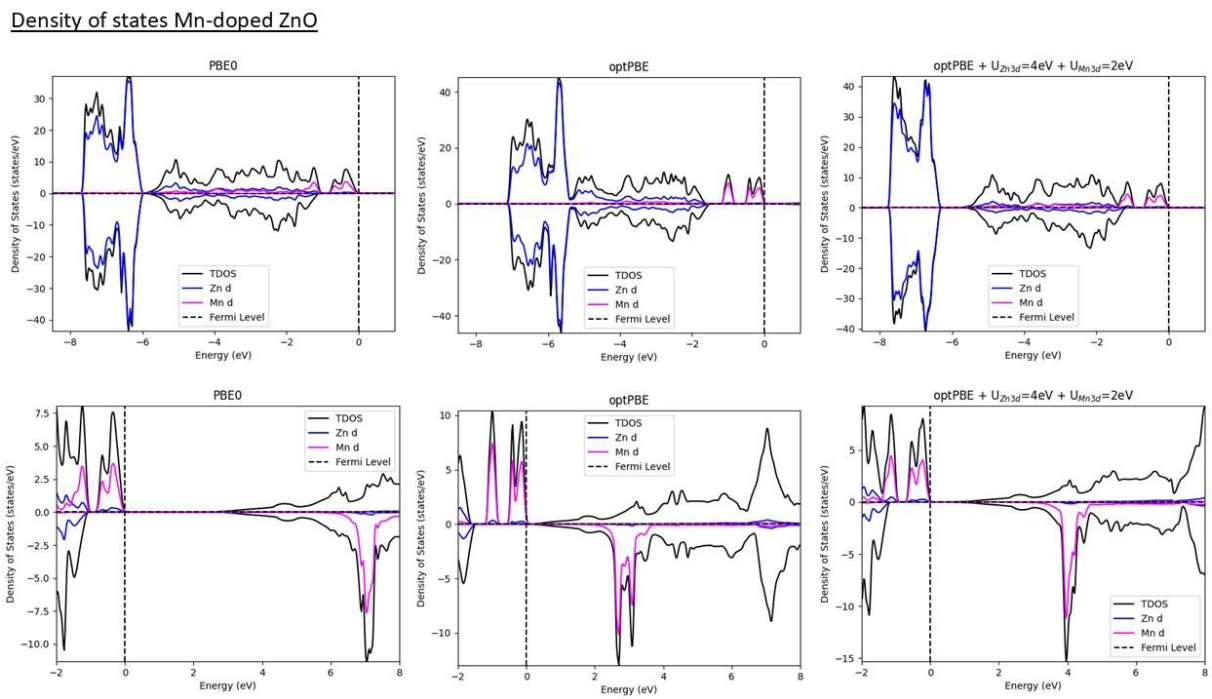

Figure A.3 Density of states analysis for Mn-doped ZnO using PBE0, optPBE, and optPBE + U (UZn-d = 4, UMn-d = 2). Each column shows the TDOS and PDOS for Zn d and Mn d orbitals under the corresponding functionals. The Fermi level is set at 0 eV.

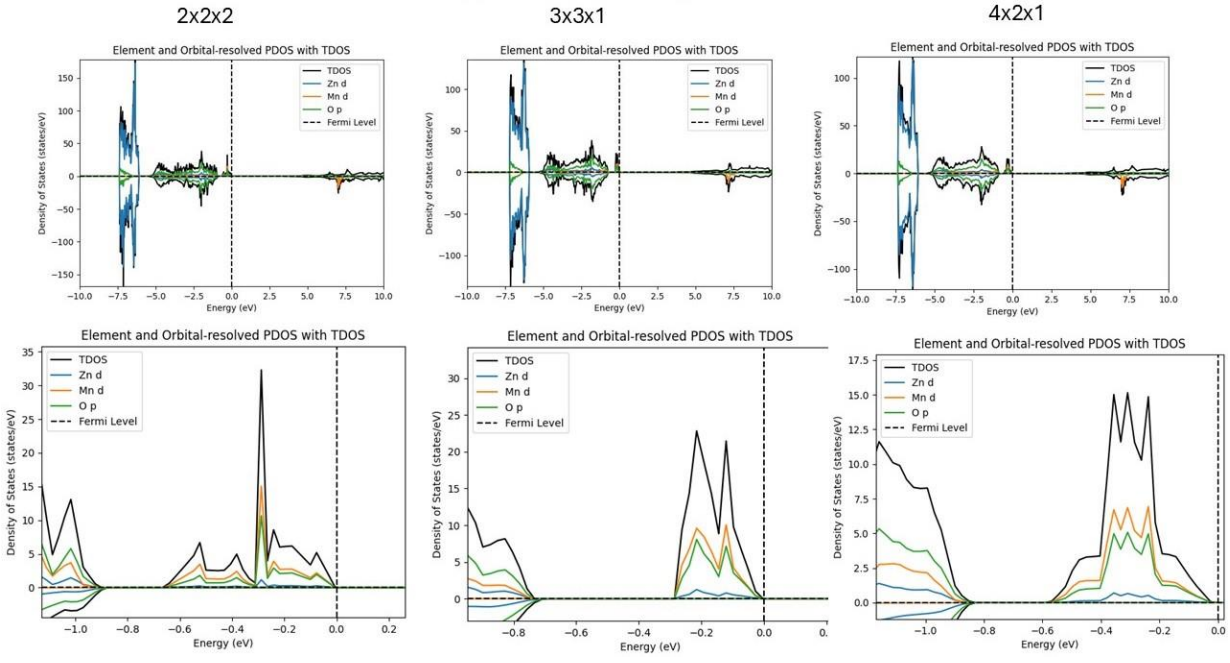

Figure A.4 Element- and orbital-resolved partial density of states (PDOS) and total density of states (TDOS) for Mn-doped ZnO calculated using the PBE0 functional across three supercells: 2×2×2, 3×3×1, and 4×2×1. The top row shows full spin-resolved PDOS over a wide energy range, while the bottom row presents zoomed-in views near the Fermi level.

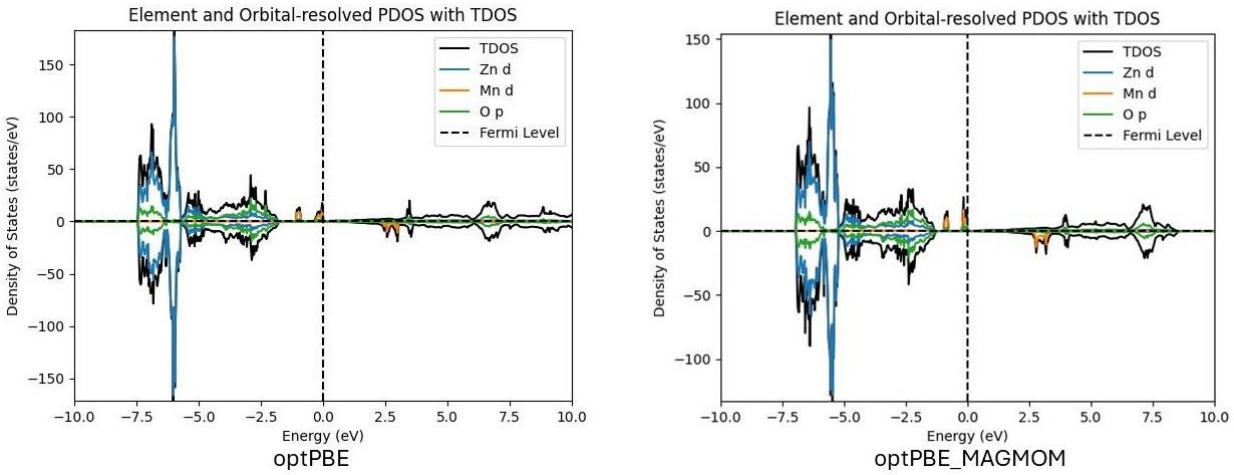

Figure A.5 Element- and orbital-resolved partial density of states (PDOS) and total density of states (TDOS) for Mn-doped ZnO 3x3x1 supercell using the optPBE functional. The left panel corresponds to a calculation without magnetic moment initialization, while the right panel includes MAGMOM initialization.

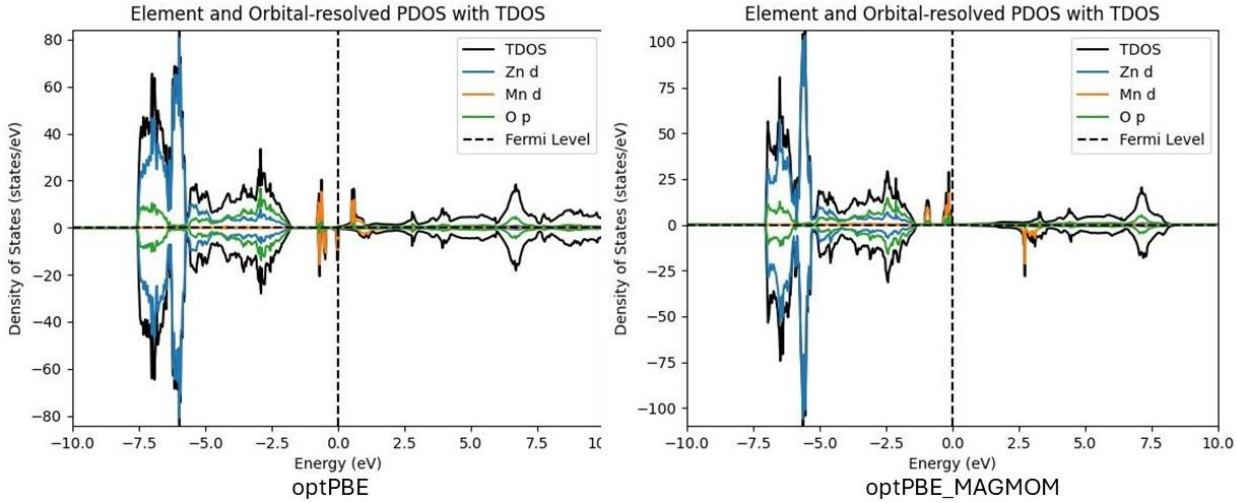

Figure A.6 Element- and orbital-resolved partial density of states (PDOS) and total density of states (TDOS) for Mn-doped ZnO 4x2x1 supercell using the optPBE functional. The left panel corresponds to a calculation without magnetic moment initialization, while the right panel includes MAGMOM initialization.